http://dx.doi.org/10.1070/RCR4928

$Ba(Ce,Zr)O_3$-based electrodes for protonic ceramic electrochemical cells: towards highly compatible functionality and triple-conducting behaviour

Anna V. Kasyanova,[a, b] Liana R. Tarutina,[a] Anna O. Rudenko,[a] Julia G. Lyagaeva,[a, b] Dmitry A. Medvedev [a, b]

[a] Institute of High Temperature Electrochemistry, the Ural Branch of the Russian Academy of Sciences, ul. Academicheskaya 20, 620137 Yekaterinburg, Russian Federation
[b] Ural Federal University named after the First President of Russia B.N.Yeltsin, ul. Mira 19, 622002 Yekaterinburg, Russian Federation

Protonic ceramic fuel cells and electrolysis cells represent low- and intermediate-temperature electrochemical devices, which allow chemical-to-electrical energy conversion with very high efficiency and low environmental impact. In order to ensure the long-term operability of these devices, as well as to provide for their up-scaling, a number of existing challenges associated with chemical and thermal incompatibilities pertaining to the functional materials remain to be overcome. This work presents a comprehensive overview of new electrode materials based on barium cerate/zirconate. The structural fragments of these materials are similar to those of the proton-conducting $Ba(Ce,Zr)O_3$ electrolytes, which causes superior chemical compatibility between different functional materials. The primary emphasis of the research is on the functional properties of these materials such as chemical stability, thermal expansion behaviour and transport features. This in turn determines the electrochemical performance of the designed electrodes. In addition, the possibility of obtaining triple-conducting materials is discussed as means of designing electrodes with a high electrochemical active surface area required for the design of high-performance protonic ceramic fuel and electrolysis cells.
The bibliography includes 208 references.

Contents

1. Introduction 667
2. General overview 669
   2.1. Crystal structure features 669
   2.2. Defect chemistry 670
   2.3. Functional properties of oxygen (steam) electrodes 671
   2.4. Justification for the design of $Ba(Ce,Zr)O_3$-based electrodes 672
3. Functionality of the M-doped $Ba(Ce,Zr)O_3$ materials 672
   3.1. Phase structure 672
   3.2. Chemical compatibility with the proton-conducting electrolytes 675
   3.3. Thermo-mechanical and chemo-mechanical behaviour 675
   3.4. Hydration capability 677
   3.5. Electrical conductivity 679
4. Performance of the M-doped $Ba(Ce,Zr)O_3$ electrodes 681
   4.1. Electrochemical activity features 682
   4.2. Symmetrical cells 682
   4.3. Protonic ceramic fuel cells 683
5. Degradation features 686
6. Future prospects and concluding remarks 688

1. Introduction

Proton-conducting materials based on complex oxides are extensively studied, being of great interest in terms of both fundamental and applied science.[1 – 5] At elevated temperatures, such oxide systems, which are naturally free from hydrogen in any form, have the potential to interact with the hydrogen-containing components of a gas atmosphere, resulting in the production of protons. Due to their beneficial crystallochemical characteristics, some complex oxides allow the formation of a high concentration of protons, which can result in predominantly protonic transportation.[6] This feature represents applied advantages compared with conventional oxygen-ionic conductors due to the lower potential barrier and higher mobility of protons. As a result, such proton-conducting materials provide a good basis for

Received 6 November 2019
© 2020 Uspekhi Khimii, ZIOC RAS, Russian Academy of Sciences and IOP Publishing Limited

the fabrication of various electrochemical cells. Currently, a proton-conducting sign has been revealed for numerous compounds based on such parent phases as $La(Y,Yb)O_3$,[7,8] $LaScO_3$,[9] $CaZrO_3$,[10] $SrCeO_3$,[11] $SrZrO_3$,[12] $Ba_2In_2O_5$,[13] $Ba_2CaNbO_{5.5}$,[14] $LaNbO_4$,[15] $La_2Ce_2O_7$,[16] $La_2Zr_2O_7$,[17] La_6MoO_{12},[18] *etc*. Among them the materials based on $BaCeO_3$ (cerates) or $BaZrO_3$ (zirconates) have been broadly studied as one of the most pronounced proton conductors.[1–6]

From the viewpoint of their potential operation across low- and intermediate-temperature ranges, protonic ceramic fuel cells (PCFCs) and protonic ceramic electrolysis cells (PCECs) compete with cells based on oxygen-conducting electrolytes, *i.e*. solid oxide fuel cells (SOFCs) and solid oxide electrolysis cells (SOECs).[1–5] Since their mode of energy conversion approaches single-step, resulting in quite high overall efficiency, PCFCs and PCECs are promising electrochemical systems.[19,20] Due to their high theoretical attractiveness for developing hydrogen and electrochemical energy fields, the problem of obtaining high practical performance and corresponding long-term stability is becoming increasingly urgent as a means of ensuring the future commercialisation of PCFCs/PCECs.

One of the possible approaches for achieving excellent operational conditions in electrochemical systems lies in careful modification of the electrode materials, which must satisfy a number of strict requirements:[21–24] phase stability, chemical compatibility, suitable thermo- and chemico-mechanical properties, high electronic conductivity, acceptable ionic transportation, high tolerance to poisoning and, finally, excellent electrochemical (electrocatalytic) performance. In this regard, various single-phase oxides, composite materials and heterogeneous systems have been successfully adopted as oxygen or steam electrodes to provide oxygen reduction (ORR) and water evolution (WER) reactions, which determine the overall efficiency and performance of low- and intermediate-temperature PCFCs/PCECs based on thin-film electrolytes.[25–27] Among existing alternatives, the design of electrodes based on $BaCeO_3$, $BaZrO_3$ or $Ba(Ce,Zr)O_3$ and doped with transition elements is considered as one of the contemporary trends. This is due to a synergetic effect: on the one hand, a basic perovskite structure is maintained to provide possible proton transportation as well as superior chemical and mechanical compatibilities with the corresponding electrolytes; on the other hand, the existence of redox-active elements in large quantities results in enhanced electrical and electrochemical properties.

Although many review articles have been published in the last few years, they describe different aspects of proton-conducting electrolytes, including proton transportation behaviour,[1,2] materials design,[4,6] technological issues[28,29] or application features.[3,15,30,31] In this brief review, we highlight the recent achievements in the design and development of PCFCs and PCECs, the functional components of which are based on the same fragmentary type of ABO_3 (A = Ba, B = Ce, Zr or Ce/Zr). In particular, the main focus of the present review is directed towards the functional properties of M-doped ABO_3 materials (M is a transition element) which can serve not as electrolytes, but as electrodes of PCFCs and PCECs and their role in the achievement of the target performance of the electrochemical devices.

In this review work, the following designations and abbreviations are used:

Abbreviations:

D — oxygen diffusion coefficient,
DD — degradation degree,
DR — degradation rate,
MIECs — mixed ionic-electronic conductors,
OCV — open circuit voltage,
ORR — oxygen reduction reaction,
PCFCs — protonic ceramic fuel cells,
PCECs — protonic ceramic electrolysis cells,
SOFCs — solid oxide fuel cells,
SOECs — solid oxide electrolysis cells,
TEC — thermal expansion coefficient,
TG — thermogravimetry,
TPB — triple phase boundary,
WER — water evolution reaction,
XRD — X-ray diffraction,
sp. gr. — space group.

Symbols:

k — oxygen surface exchange constant,
M — transition element,
R — acceptor dopant,
R_o — ohmic resistance,
R_p — polarisation resistance,
R_{total} — total resistance,
P_{max} — maximal power density,
p_{O_2} — oxygen partial pressure,
p_{H_2O} — water vapour partial pressure,
T — temperature,
r_A, r_B and r_O — ionic radii of A-, B- and O-ions, respectively,
t — Goldschmidt's tolerance factor,
α — the TEC value,
δ — oxygen stoichiometry,
η — overpotential.

Defect notation:

$h^{\bullet}$ — electronic holes,
e' — electrons,
O_O^x — oxide ion at the normal oxygen site,
$OH_O^{\bullet}$ — proton defects,
$R'_{Ce(Zr)}$ — acceptor dopant localised in the Ce(Zr) sublattice,
$V_O^{\bullet\bullet}$ — oxygen vacancies.

Composition designations:

ABO_3 — perovskite structure,
$Ba(Ce,Zr)O_3$ — general system of the considered materials, $BaCeO_3 - BaZrO_3$, which include boundary composi-

A.V.Kasyanova. Master student, Junior Researcher at the Laboratory of Electrochemical Devices Based on Solid Oxide Proton Electrolytes, IHTE UB RAS. ORCID: 0000-0002-3662-6051
Telephone: +7(343)362–3130, e-mail: kasyanova.1996@list.ru
L.R. Tarutina. Ph.D. student, engineer at the same Laboratory. ORCID: 0000-0003-1079-5292
Telephone: +7(343)362–3130, e-mail: hakimovaliana@rambler.ru
A.O. Rudenko. Engineer at the same Laboratory. ORCID: 0000-0003-3563-8832
Telephone: +7(343)362–3642, e-mail: nikusa28@mail.ru
J.G. Lyagaeva. Candidate of Science in Chemistry, Senior Researcher at the same Laboratory. ORCID: 0000-0003-4496-3768
Telephone: +7(343)362–3642, e-mail: yulia.lyagaeva@ya.ru
D.A. Medvedev. Doctor of Science in Chemistry, Leading Researcher at the same Laboratory. ORCID: 0000-0003-1660-6712
Telephone: +7(343)362–3202, e-mail: dmitrymedv@mail.ru
Current research interest of the authors: energy conversion processes and technologies, designing solid oxide materials for high-temperature applications, fabrication and characterisation of solid oxide electrochemical systems (fuel cells, electrolysis cells, sensors, membrane reactors).

tions ($BaCeO_3$, $BaZrO_3$), solid solutions ($BaCe_{1-x}Zr_xO_3$) as well as doped or co-doped derivatives,

$Ba(Ce,Zr,R)O_3$ — same as above, but doped with R-dopant(s),

BCB — $BaCe_{0.5}Bi_{0.5}O_{3-\delta}$

BCCY — $BaCo_{0.7}(Ce_{0.8}Y_{0.2})_{0.3}O_{3-\delta}$,

BCCY′ — $BaCe_{0.7}Co_{0.2}Y_{0.1}O_{3-\delta}$,

BCF — $BaCe_{0.5}Fe_{0.5}O_{3-\delta}$,

BCFB — $BaCe_{0.5}Fe_{0.3}Bi_{0.2}O_{3-\delta}$,

BCFBx — $BaCe_{0.5}Fe_{0.5-x}Bi_xO_{3-\delta}$ (x = 0, 0.1, 0.2 and 0.3)

BCFC — $BaCo_{0.4}FeCe_{0.1}O_{3-\delta}$,

BCFZ — $BaCo_{0.4}Fe_{0.4}Zr_{0.2}O_{3-\delta}$,

$B_{0.9}$CFZY — $Ba_{0.9}Co_{0.4}Fe_{0.4}Zr_{0.1}Y_{0.1}O_{3-\delta}$,

BCFZY — $BaCo_{0.4}Fe_{0.4}Zr_{0.1}Y_{0.1}O_{3-\delta}$,

BCP — $BaCe_{0.6}Pr_{0.4}O_{3-\delta}$,

BCS — $BaCe_{0.8}Sm_{0.2}O_{3-\delta}$

BCSC — $BaCe_{0.4}Sm_{0.2}Co_{0.4}O_{3-\delta}$,

BCSF — $BaCe_{0.4}Sm_{0.2}Fe_{0.4}O_{3-\delta}$,

BCxFZ — $BaCo_xFe_{0.7-x}Zr_{0.3}O_{3-\delta}$ (x = 0.2, 0.3, 0.4 and 0.5),

BCFCG — $BaCo_{0.4}Fe_{0.4}Ce_{0.1}Gd_{0.1}O_{3-\delta}$,

BCZY — $BaCe_{0.7}Zr_{0.1}Y_{0.2}O_{3-\delta}$,

BCZYYb — $BaCe_{0.7}Zr_{0.1}Y_{0.1}Yb_{0.1}O_{3-\delta}$,

BFCC — $BaFe_{0.6}Co_{0.3}Ce_{0.1}O_{3-\delta}$,

BFSB — $BaFe_{0.5}Sn_{0.2}B_{0.3}O_{3-\delta}$,

BSCF — $Ba_{0.5}Sr_{0.5}Co_{0.8}Fe_{0.2}O_{3-\delta}$,

BZY — $BaZr_{0.8}Y_{0.2}O_{2-\delta}$,

BZCY35 — $BaZr_{0.3}Ce_{0.5}Y_{0.2}O_{3-\delta}$,

BZCY442 — $BaZr_{0.4}Ce_{0.4}Y_{0.2}O_{3-\delta}$,

BZCY63 — $BaCe_{0.6}Zr_{0.3}Y_{0.1}O_{3-\delta}$,

BZC64 — $BaZr_{0.6}Co_{0.4}O_{3-\delta}$,

BZCC — $BaZr_{0.1}Ce_{0.7}Co_{0.2}O_{3-\delta}$,

BZF0.6Y — $BaZr_{0.2}Fe_{0.6}Y_{0.2}O_{3-\delta}$,

BZFxY — $BaCo_{0.8-x}Fe_xY_{0.2}O_{3-\delta}$ (x = 0.2, 0.4, 0.6 and 0.8),

LCSF — $La_{0.6}Sr_{0.4}Co_{0.2}Fe_{0.8}O_{3-\delta}$,

LSM — lanthanum strontium manganite, $La_{1-x}Sr_xMnO_{3-\delta}$,

PBC — $PrBaCo_2O_{5+\delta}$,

SDC — $Ce_{0.8}Sm_{0.2}O_{2-\delta}$,

YSZ — yttria-stabilised zirconia, $Zr_{1-x}Y_xO_{2-\delta}$.

2. General overview

2.1. Crystal structure features

The ABO_3 perovskite structure represents one of the largest bases for oxide materials utilised at elevated temperatures. The ABO_3 structure possesses a high flexibility allowing accommodation of different cations at the A- and B-site positions.[32] As a result, all types of conductors (predominantly ionic, predominantly electronic, mixed ionic-electronic) can be formed depending on different charge combinations of basic cations (A^+/B^{5+}, A^{3+}/B^{3+}, A^{2+}/B^{4+}), as well as their redox behaviour and ionic radii.

In general, it is possible to evaluate the stability of perovskite structures using the Goldschmidt's tolerance factor (Eqn 1), which is based on the geometrical consideration of structural fragments of ABO_3.[33]

$$t = \frac{r_A + r_O}{\sqrt{2}(r_B + r_O)} \quad (1)$$

where r_A, r_B and r_O are the corresponding radii of A-, B- and O-ions in the corresponding coordination states.

Using experimental data for a large number of oxide materials, it is found that the perovskite structure forms when the t value drops to within the range of 0.71 – 1.06. If this factor is close to 1.00, a cubic symmetry emerges; otherwise, different distortions of ABO_3 are observed with a deviation of t from unity.[34]

$BaCeO_3$ and $BaZrO_3$ belong to the perovskite-structured materials (Fig. 1 *a*). Barium as an alkaline-earth element with a large ionic radius occupies the A-site of ABO_3, being coordinated by twelve neighbouring oxygen ions. Cerium or zirconium, having lower ionic radii, is placed in the B-sublattice of ABO_3, where six oxygen ions form a B-centred octahedra. Using Shannon's ionic radii,[35] the t value of $BaCeO_3$ and $BaZrO_3$ amounts to 0.938 and 1.004, respectively. Under experimental conditions, a doped $BaZrO_3$ can be seen to adopt a cubic-type perovskite structure at room temperature (Fig. 1 *b*), whose stability extends up to 1600 °C.[36] Conversely, an orthorhombic structure is most frequently observed for pure $BaCeO_3$, which, however, can transform to monoclinic, rhombohedral or even cubic structures at normal conditions depending on nature of

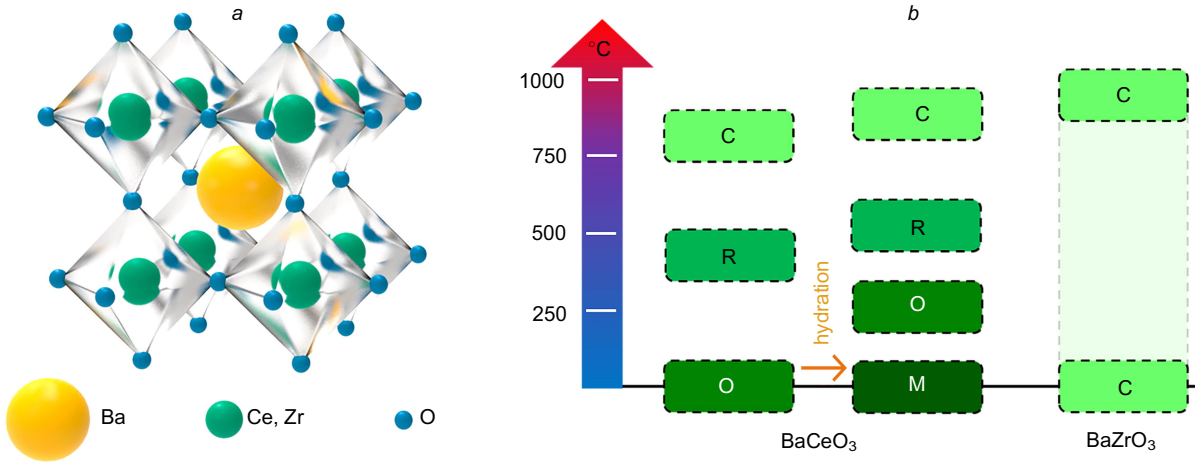


Figure 1. General perovskite structure of the $Ba(Ce,Zr)O_3$-based materials (*a*) and its evolution with heating (*b*). Abbreviations: M — monoclinic, O — orthorhombic, R — rhombohedral, C — cubic.

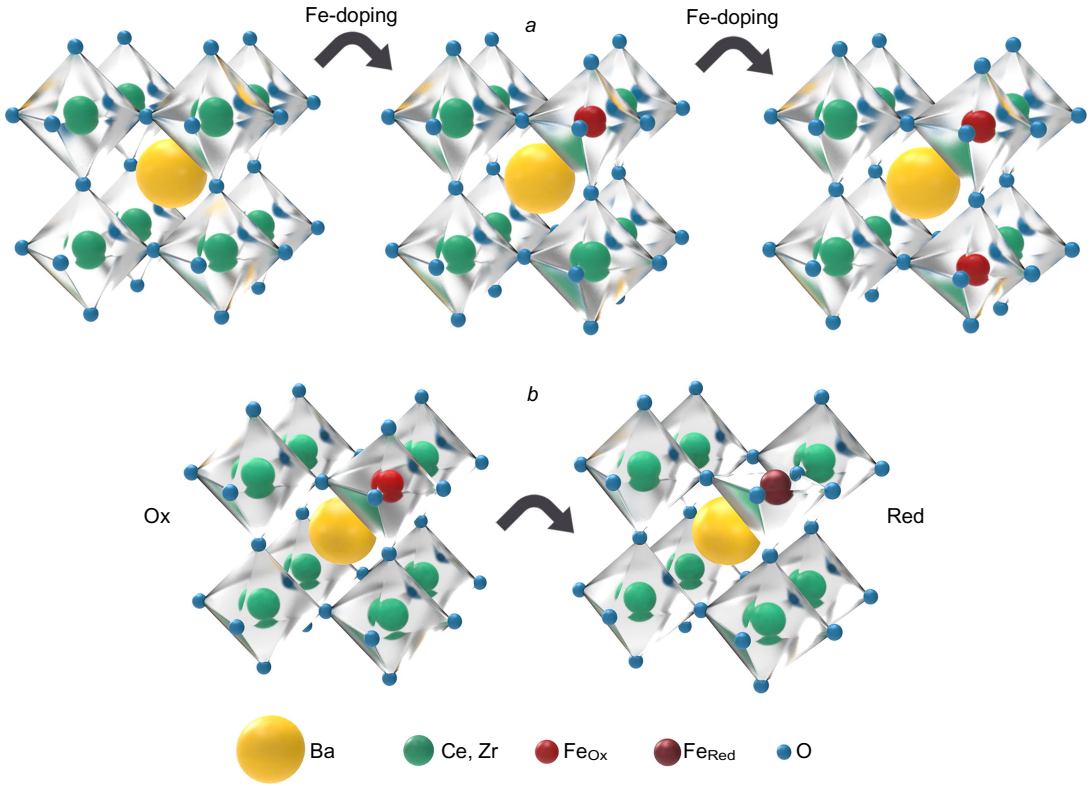


Figure 2. Schematic representations of the gradual Fe-doping of $Ba(Ce,Zr)O_3$ (*a*) and reduction of the obtained products (*b*).

dopants, their concentration and/or degree of hydration (Fig. 1 *b*).[37–39]

2.2. Defect chemistry

When $BaCeO_3$ or $BaZrO_3$ is doped with elements having a constant oxidation state ($R = Ln^{3+}$, Sc^{3+}, In^{3+}, Y^{3+}), a wide range of solid solutions can be formed. These oxides are used as a basis for designing electrolyte materials having a predominantly ionic conducting behaviour. In details, such a doping causes the formation of oxygen vacancies ($V_O^{\cdot\cdot}$):

$$R_2O_3 \xrightarrow{'(Ce,Zr)O_2'} 2\,R'_{Ce(Zr)} + V_O^{\cdot\cdot} + 3\,O_O^x \qquad (2)$$

The oxygen vacancies compensate for the defects with an effective negative charge ($R'_{Ce(Zr)}$) and govern the oxygen-ionic transport of $BaCeO_3$- and $BaZrO_3$-based materials when these oxides are not significantly hydrated (low water vapour partial pressures, very high temperatures) or protonic transport (by means of proton defects, $OH_O^{\cdot}$) emerging in other cases, including at low temperatures coupled with high water vapour partial pressures:[40–42]

$$H_2O + V_O^{\cdot\cdot} + O_O^x \rightleftarrows 2\,OH_O^{\cdot} \qquad (3)$$

Along with ionic transportation, cerates and zirconates show electronic transport on account of hole- (Eqn 4) or electron (Eqn 5) charge carriers, which can make a considerable contribution to overall transport under oxidising and reducing conditions, respectively.[43–45]

$$\frac{1}{2}O_2 + V_O^{\cdot\cdot} \rightleftarrows 2\,h^{\cdot} + O_O^x \qquad (4)$$

$$O_O^x \rightleftarrows \frac{1}{2}O_2 + 2\,e' + V_O^{\cdot\cdot} \qquad (5)$$

On the basis of experimental results, p-type electronic conductivity can be seen to emerge at oxidising conditions above 500 °C and then rapidly increase with heating, starting to predominate over other partial (oxygen-ionic, protonic) conductivities at temperatures higher than 700 – 800 °C.[6] Considering n-type electronic conductivity, it is possible that this originates under strongly reduced atmospheres (very low oxygen partial pressures, p_{O_2}†) on account of the partial reduction of Ce^{4+}-ions:

$$2\,Ce_{Ce}^x + O_O^x \rightleftarrows 2\,Ce'_{Ce} + V_O^{\cdot\cdot} + \frac{1}{2}O_2 \qquad (6)$$

The equilibrium constant of this reaction varies from 10^{-42} at 400 °C to 10^{-17} at 800 °C, leading to a very low contribution of n-type electronic conductivity under real experimental conditions.[46]

The total conductivity of the considered ceramic materials attains moderate values (not more than 0.1 S cm^{-1} at 900 °C)[47,48] despite the gas compositions used. Due to this fact, the $BaCeO_3$- or $BaZrO_3$-based materials are mostly considered as electrolytes of protonic ceramic electrochemical cells. However, the electronic transport can be deliberately enhanced using elements with transition oxidation states (M), forming as-called mixed ionic-electronic conductors, MIECs.[49–51] If the M-elements can substitute the basic ions of ABO_3 to form single-phase derivatives (Fig. 2 *a*), the transport properties of the materials depend

† Here and below partial pressures are provided in relative units (*i.e.* they are normilized to $P = 1$ atm).

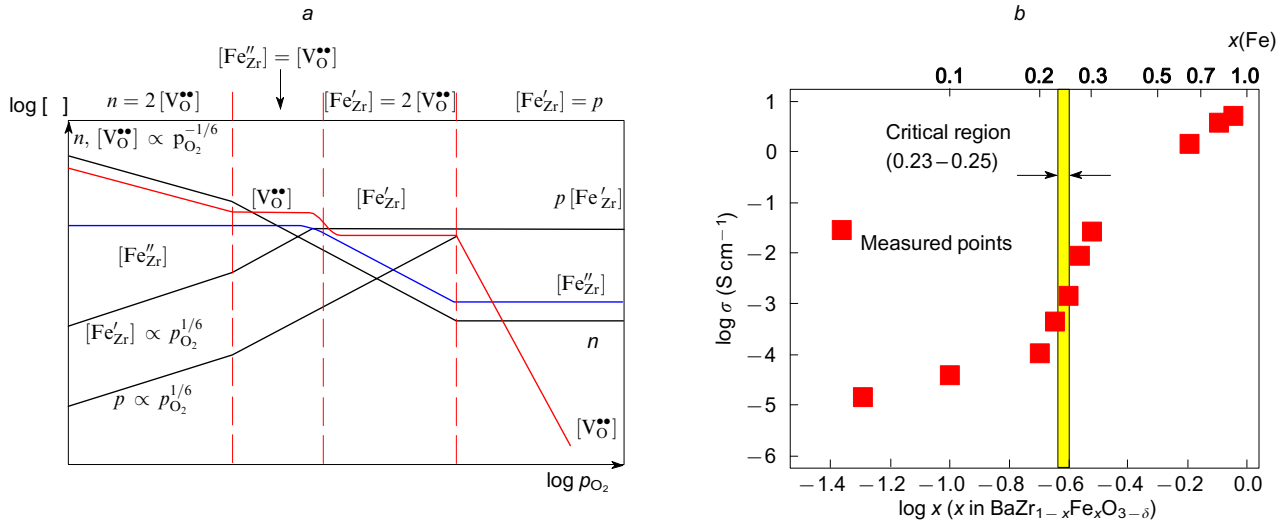


Figure 3. Transport properties of $BaZr_{1-x}Fe_xO_{3-\delta}$ materials: (*a*) concentrations of existing defects depending on oxygen partial pressure for $x = 0.1$ at 800 °C;[52] (*b*) concentration dependence of the total conductivity obtained at 500 °C in dry O_2 ($p_{O_2} = 1$).[54] Designations: [ ] brackets denote concentration of defects, n is the concentration of electrons, p is the concentration of holes, $V^{\bullet\bullet}_O$ is the oxygen vacancy, Fe'_{Zr} is the Fe^{3+}-ion located at the zirconium sublattice of $BaZrO_3$, Fe''_{Zr} is the Fe^{2+}-ion located at the zirconium sublattice of $BaZrO_3$, p_{O_2} is the oxygen partial pressure, x is the level of Fe-doping of $BaZrO_3$, σ is the total conductivity.

on the charge conditions of M-ions, which are regulated by the external factors. For example, in the model $BaZr_{1-x}Fe_xO_{3-\delta}$ system, the Fe-ions can be consequently reduced by decreasing the oxygen partial pressure (Fig. 3 *a*, ref. 52), forming first the Fe^{3+}-ions (Eqn 7) and then Fe^{2+}-ions (Eqn 8).

$$2\,Fe^{x}_{Zr} + O^{x}_{O} \rightleftharpoons 2\,Fe'_{Zr} + V^{\bullet\bullet}_O + \frac{1}{2}O_2 \quad (7)$$

$$2\,Fe'_{Zr} + O^{x}_{O} \rightleftharpoons 2\,Fe''_{Zr} + V^{\bullet\bullet}_O + \frac{1}{2}O_2 \quad (8)$$

Here, Fe^{x}_{Zr} and Fe''_{Zr} are holes and electrons localised at the Fe'_{Zr}-ions. An additional equation (which is equivalent to the hole/electron interaction, null $\rightleftharpoons h^{\bullet} + e'$) links all of these defects:

$$2\,Fe'_{Ce} \rightleftharpoons Fe''_{Ce} + Fe^{x}_{Ce} \quad (9)$$

The reduction of the elements with transition oxidation states results in changes in the crystal structure (Fig. 2 *b*, Ref. 53), consisting in chemical strain effects: an increase in the ionic radius of M-ions and removal of oxygen from its regular crystal position. Both of these outcomes affect the functional properties of the materials. For example, the conductivity caused by an increase in the concentration of electron charge carriers by doping with transition elements is not monotonic (Fig. 3 *b*, Ref. 54). As a result of changes in the transportation mechanism, a percolation-type behaviour is observed: the p-type electron conductivity at low M concentrations is managed by transportation of holes localised at oxygen ions, while at higher M concentrations it is provided by holes localised at M-cations. Therefore, with a gradual growth of the M concentration, the total conductivity increases slightly [54] (or even decreases),[55,56] but then rises rapidly to reach 1–10 S cm^{-1}. From this perspective, the priority should be given the $Ba(Ce,Zr)O_3$-based systems containing more than 40 mol. % of M in the Ce/Zr-positions.

2.3. Functional properties of oxygen (steam) electrodes

The electrode materials utilised in PCFCs or PCECs must fulfil strict requirements determining the overall performance of the electrochemical systems. There are various terms used to describe electrode performance: overpotential (η), area specific resistance or polarisation resistance (R_p). In this work, the latter term will be used for convenience. The R_p parameter depends on different factors,[57–62] which can be categorised in two main groups (Fig. 4): chemical and morphological stabilities. In turn, these factors control (electro)catalytic activity of the electrode material as well as excellent exchange transport through the interfaces.

Chemical stability comprises all aspects of a material's stability, such as long-term tolerance, chemical compatibility with the electrolyte, electrode tolerance to poisoning by gas phase components, *etc*. The morphological stability group includes problems associated with the delamination process, coarsening of particles, *etc*. On the one hand, the mentioned drawbacks result in the deterioration of electrical contacts [decreasing triple phase boundary (TBP), active electrode area or porosity]; on the other hand, ionic and electronic current fluxes are also decreased. Various strategies can be deliberately utilised for the suppression of such undesirable processes.[63–67] One of these is to develop

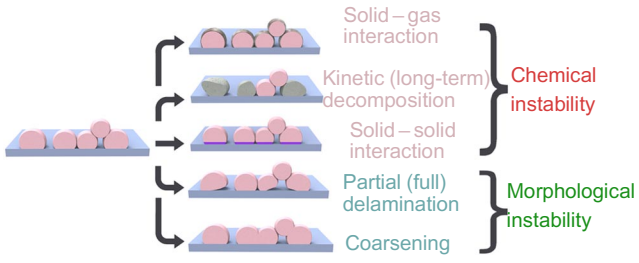


Figure 4. Possible reasons for increasing polarisation resistance of the electrodes in electrochemical systems.

electrodes having the same basic structure as the used electrolyte and consequently exhibiting a high chemical compatibility with it.

2.4. Justification for the design of Ba(Ce,Zr)O_3-based electrodes

The design of electrodes based on barium cerate or barium zirconate allows many problems to be overcome. Firstly, this approach can increase chemical compatibility since both functional [M-doped Ba(Ce,Zr)O_3 and R-doped Ba(Ce,Zr)O_3] materials are composed of the same structural fragments. In other words, the degree of possible interaction decreases considerably due to its being determined by the chemical activity of M- and R-cations with respect to each other. Thermal compatibility can also be improved by means of ensuring similar thermochemical strain responses. On account of their large perovskite structure, as well as the basic properties of Ba^{2+}-, Ce^{4+}- and Zr^{4+}-cations, M-doped oxides might show hydration behaviour along with meaningful oxygen-ionic and electronic transport caused by M-cations. Such a combination opens new opportunities for the formation of single-phase triple-conducting materials, which are highly appreciated for their utilisation in protonic ceramic electrochemical cells.[68–70] In detail, triple-conduction behaviour extends the electrochemical active sites from the TPB to the entire surface of the electrode particles, see Fig. 5.

As illustrated in Fig. 5 *a*, in two protonic and electronic conductors when three phases of provided transportation of electrons (electrode), protons (electrolyte) and oxygen (gas atmosphere) exist simultaneously, the electrochemical reduction process is limited by the TPB region, see Eqn 10. In cases where MIECs are applied (Fig. 5 *b*), the oxygen reduction stage occurs over the entire electrode surface (Eqn 11). However, the resulting water evolution reaction stage is still limited by the TPB length (Eqn 12). Eventually, the entire surface of the electrode becomes active towards both ORR and WER (Fig. 5 *c*, Eqs. 10–13), extending the electrochemically active region from the length of the TPB to the surface of the double-phase boundary, *i.e.* the electrode's surface. However, in order to ensure sufficient rates of ORR and WER, the electrode materials should have high levels of each partial conductivity. Otherwise, the limiting cases (electronic conductors or MIECs) will be realised.

$$2H^{+}_{electrolyte} + \frac{1}{2}O_{2\,gas} + 2e'_{electrode} \longrightarrow H_2O_{gas} \quad (10)$$

$$\frac{1}{2}O_{2\,gas} + 2e'_{electrode} \longrightarrow O^{2-}_{electrode} \quad (11)$$

$$2H^{+}_{electrolyte} + O^{2-}_{electrode} \longrightarrow H_2O_{gas} \quad (12)$$

$$2H^{+}_{electrode} + O_{ads,\,electrode} + 2e'_{electrode} \longrightarrow H_2O_{gas} \quad (13)$$

3. Functionality of the M-doped Ba(Ce,Zr)O_3 materials

Amongst the wide variety of oxide compositions, Ba(Ce,Zr)O_3 doped with praseodymium, cobalt and iron have been most thoroughly studied. Therefore, the main emphasis is devoted to such materials and their individual properties: phase structure, mechanical and chemical compatibilities, hydrogen capability and electrical conductivity.

3.1. Phase structure

The phase structure of the ABO_3 perovskites depends on numerous factors, including A and B matrix cations, concentration and type of dopants, their redox properties, cationic and anionic nonstoichiometry and even technological factors (temperatures of high-temperature treatments, dwelling times).[32–34] When barium occupies the A-sublattice, while Ce or Zr occupy the B-sublattice, single-phase materials of $BaCeO_3$ having orthorhombic structure and $BaZrO_3$ with cubic structure are stable at room temperature, as discussed in detail in Section 2.1.

In case of Ba(Ce,Zr)O_3 doped with the M-transition elements, different results can be obtained in terms of the phase structure and purity of the obtained derivatives (see Table 1).

When Fe-doping is used with the $BaCeO_3$-based system, a limited range of solid solutions forms. According to numerous works,[71, 72, 74, 75, 83] two ranges of solid solutions exist in the $BaCe_{1-x}Fe_xO_{3-\delta}$ system, which are limited by compositions with $x \approx 0.15$ and 0.85. Such a low solubility limit can be explained by the high differences in ionic radii between the basic (Ce^{4+}, $r^{VI}_{Ce^{4+}} = 0.87$ Å, here the superscript denotes the coordination state) and guest (iron, $r^{VI}_{Fe^{4+}} = 0.585$ Å, $r^{VI}_{Fe^{3+}} = 0.645$ Å) cations, which cause energetically unfavourable conditions. A similarly limited range for the heavy Fe-doped oxides ($0.85 \leqslant x \leqslant 1$) confirms this assumption. As shown by Eqn 1, a decrease in the average ionic radii of the B-ions leads to an increase in the tolerance factor; this implies that the overall stability of the perovskite structure (and its symmetry) should also increase, namely in the range of single-phase materials. Indeed, $BaCe_{0.85}Fe_{0.15}O_{3-\delta}$ has an orthorhombic perovskite structure,[75] while a hexagonal structure is detected for the nominal $BaCe_{0.4}Sm_{0.2}Fe_{0.4}O_{3-\delta}$ composition[71] and $BaCe_{0.15}Fe_{0.85}O_{3-\delta}$ exhibits a cubic-type perovskite structure.[75]

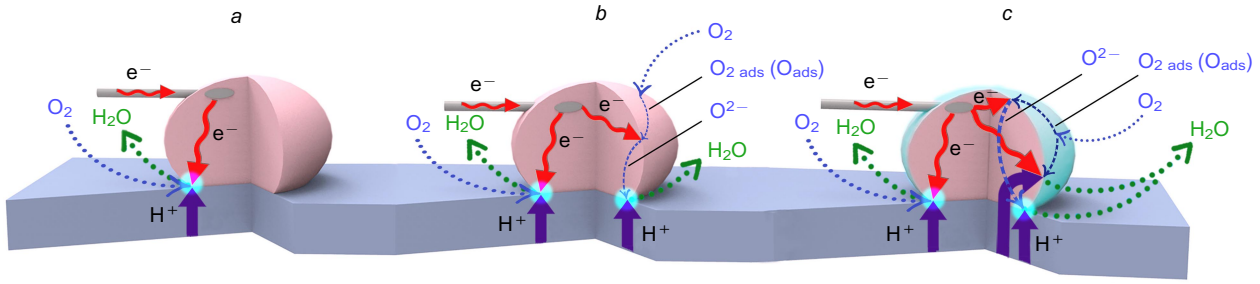


Figure 5. Simplified scheme of the electrochemically active sites in PCFCs with electronic (*a*), mixed oxygen-ionic/electronic (*b*) and triple (*c*) conducting electrodes. These sites are highlighted by a colour.

Table 1. Powder synthesis method, sintering conditions and crystal structures of various perovskite cathodes based on $Ba(Ce,Zr)O_3$.

Composition	Synthesis method	Sintering conditions:		Phase structure	Ref.
		T/ °C	τ/ h		
		Fe-doped $Ba(Ce,Zr)O_3$			
$BaCe_{0.4}Sm_{0.2}Fe_{0.4}O_{3-\delta}$	Combined EDTA – citrate complexing sol – gel	900 1100	10 10	Dual phase system: $BaCe_{1-x}(Sm/Fe)_xO_{3-\delta}$ and $BaFe_{1-y}(Sm/Ce)_yO_{3-\delta}$ with orthorhombic and hexagonal structures, respectively	71, 72
$BaZr_{0.9}Fe_{0.1}O_{3-\delta}$	Solid state synthesis	1150	5	Cubic structure	73
$BaCe_{0.5}Fe_{0.5}O_{3-\delta}$	Combined EDTA – citrate complexing sol – gel	900 950 100	2 2 2	Dual phase system: $BaCe_{0.15}Fe_{0.85}O_{3-\delta}$ and $BaCe_{0.85}Fe_{0.15}O_{3-\delta}$	74
$BaCe_xFe_{1-x}O_{3-\delta}$ (x = 0.15, 0.50, 0.85)	Pechini method	1100	3	x = 0.15 — cubic structure, x = 0.50 — dual phase, x = 0.85 — orthorhombic structure	75
$BaZr_{1-x}Fe_xO_{3-\delta}$ (x = 0 – 0.9)	Pechini method	1000	6	Cubic structure	54
$BaZr_{0.85}Y_{0.1}Fe_{0.05}O_{3-\delta}$	Solid-state reaction	1400	32	Cubic structure	76
$BaZr_{0.1}Ce_{0.7}Y_{0.1}Fe_{0.1}O_{3-\delta}$	Solid-state reaction	1100 1350	12 – 24 6	Orthorhombic structure	77
$BaZr_{1-x}Fe_xO_{3-\delta}$ (x = 0.0, 0.05, 0.10, 0.20, 0.30, 0.40 and 0.50)	Sol – gel auto combustion technique	900	5	x = 0 – 0.4 — cubic structure, x = 0.5 — cubic structure with $BaCO_3$ impurity phase	78
$BaZr_{1-x}Fe_xO_{3-\delta}$ (x = 0.1, 0.2 and 0.33)	Citrate – nitrate synthesis	1000	10	x = 0 – 0.3 — cubic structure	52
$BaZr_{1-x}Fe_xO_{3-\delta}$ (x = 0 – 0.9)	Citrate – nitrate synthesis	1000	6	x = 0 – 0.3 — cubic structure, x = 0.8 — two-phase system (cubic and tetragonal structures)	79
$BaZr_{0.9-x}Yb_{0.1}Fe_xO_{3-\delta}$ (x = 0, 0.2 and 0.4)	Citrate – nitrate synthesis	1450	5	Cubic structure	80
$BaFe_{0.9}Zr_{0.1}O_{3-\delta}$	Combined EDTA – citrate complexing sol – gel method	1100	5	Cubic structure	81
$BaCe_{0.5}Fe_{0.3}Bi_{0.2}O_{3-\delta}$	Citrate – nitrate gel combustion method	1000	3	Orthorhombic structure with $BaFeO_3$-based cubic second phase	82
$BaCe_{0.5}Fe_{0.5-x}Bi_xO_{3-\delta}$ (x = 0, 0.1, 0.2 and 0.3)	Citrate – nitrate gel combustion method	1000	3	Dual phase system with both cubic and orthorhombic structures (with the increase of x, the concentration of cubic phase decreased gradually)	83
$BaCe_{0.5}Fe_{0.5-x}Bi_xO_{3-\delta}$ (x = 0.5)	Pechini method	1000	3	Single-phase material	84
		Fe and Co codoped $Ba(Ce,Zr)O_3$			
$BaFe_{0.6}Co_{0.3}Ce_{0.1}O_{3-\delta}$	Modified Pechini method	1100	3	Single-phase material	85
$BaCo_{0.4}Fe_{0.4}Zr_{0.2}O_{3-\delta}$	Combining EDTA acid and citric complexes	800 1100	5 3	Cubic structure	86
$Ba_{0.9}Co_{0.4}Fe_{0.4}Zr_{0.1}Y_{0.1}O_{3-\delta}$	EDTA citrate with combustion method	1100	3	Cubic structure	87
$BaCo_{0.4}Fe_{0.4}Zr_{0.2-x}Y_xO_{3-\delta}$ (x = 0, 0.05, 0.1, 0.15)	Sol – gel method	1000	5	Cubic structure	88
$Ba_xCo_{0.4}Fe_{0.4}Zr_{0.1}Y_{0.1}O_{3-\delta}$ (x = 1, 0.95, 0.9 and 0.85)	Combined EDTA – citricacid complexing sol – gel process	1100	5	x = 1 – 0.9 — cubic structure, x = 0.85 — cubic structure with $Co_{3-x}Fe_xO_4$ impurity	89
$BaCo_xFe_{0.7-x}Zr_{0.3}O_{3-\delta}$ (x = 0.2, 0.3, 0.4 and 0.5)	Citrate – nitrate synthesis	1050	3	Cubic structure	90
$BaFe_{0.6}Ce_{0.1}Co_{0.3}O_{3-\delta}$	Pechini method	950	5	Cubic structure	91

Table 1 (continued).

Composition	Synthesis method	Sintering conditions:		Phase structure	Ref.
		T/ °C	τ/ h		
Fe and Co codoped Ba(Ce,Zr)O_3					
$BaCo_{0.4}Fe_{0.4}Zr_{0.2}O_{3-\delta}$	Citric acid and EDTA complexing route	1100	10	Cubic structure	92
$Ba(Co_{0.4}Fe_{0.4}Zr_{0.1}Y_{0.1})_xO_{3-\delta}$ (x = 1.0, 0.975, 0.95, 0.925 and 0.90)	Sol – gel method	1000	5	Cubic structure	93
$BaCo_{0.4}Fe_{0.4}Zr_{0.2}O_{3-\delta}$	Glycerin – nitrate process	1100	4	Single-phase material	94
$BaCo_{0.7}Fe_{0.3-x}Zr_xO_{3-\delta}$ (x = 0 – 0.12)	Sol – gel method	1100	8	x = 0, 0.02 — hexagonal structure with impurities of Co_3O_4 and Fe_3O_4; x = 0.04 – 0.1 — cubic structure, x = 0.12 — cubic structure with $BaZrO_3$ impurity	95
$BaCo_{0.7}Fe_{0.2}Zr_{0.1}O_{3-\delta}$	Solid-state reaction	1100	8	Cubic structure with $BaZrO_3$ impurity	96
Co-doped Ba(Ce,Zr)O_3					
$BaZr_{0.1}Ce_{0.7}Y_{0.2-x}Co_xO_{3-\delta}$ (x = 0, 0.02, 0.05, 0.075, 0.1, 0.2)	Solid-state reaction	1100	10	$0 \leqslant x \leqslant 0.075$ — single phase, $x \geqslant 0.1$ — second phase based $BaCoO_3$	97
$BaCe_{0.9-x}Co_xY_{0.1}O_{3-\delta}$ (x = 0.05, 0.08, 0.1, 0.2)	The citric acid complex method	1100	5	x = 0.05, 0.08 — single phase, x = 0.12 — second phase based $BaCoO_3$	98
$BaCe_{0.4}Sm_{0.2}Co_{0.4}O_{3-\delta}$	Citrate – nitrate synthesis	900 1100 1200	10 10 2	Two phases of $BaCe_{1-x}(Sm/Co)_xO_{3-\delta}$ and $BaCo_{1-x}(Sm/Ce)_xO_{3-\delta}$ with trace of Ba_2CoO_4 impurity	99
$BaCo_{0.7}(Ce_{0.8}Y_{0.2})_{0.3}O_{3-\delta}$	Citrate – nitrate synthesis	–	–	Two phases of cubic perovskite phase based on $BaCo_{0.9}(Ce_{0.8}Y_{0.2})_{0.1}O_{3-\delta}$ and rhombohedral perovskite phase based on $BaCe_{0.8}Y_{0.2}O_{3-\delta}$	100
$BaZr_{0.1}Ce_{0.7}Y_{0.1}$ $Co_{0.1}O_{3-\delta}$	Solid-state reaction	1100 1350	12 – 24 6	Orthorhombic structure	77
$BaZr_{1-x}Co_xO_{3-\delta}$ (x = 0.1, 0.2, 0.3, 0.4, 0.5)	Citrate – nitrate synthesis	1100	2	$x \leqslant 0.4$ — single phase, x = 0.5 — appearance of the secondary phase of $BaCoO_3$	101
Pr-doped Ba(Ce,Zr)O_3					
$BaCe_{1-x}Pr_xO_{3-\delta}$ (x = 0.20, 0.40)	Pechini method	1000	3	Orthorhombic structure	102
$Ba(Zr_{0.7}Ce_{0.2})_{1-(x/0.9)}Pr_xY_{0.1}O_{3-\delta}$ (x = 0, 0.225, 0.445, 0.675, 0.9)	Pechini method	1350	4	Single-phase materials: x = 0.225 — sp. gr. *R*3*C*, x = 0.445 — sp. gr. *Imma*, x = 0.9 — sp. gr. *Pnma*	38
$Ba(Zr_{0.7}Ce_{0.2})_{1-x}Pr_xY_{0.1}O_{3-\delta}$ (x = 0, 0.2, 0.4, 0.6, 0.8, 1.0)	Pechini method	1350	4	Single-phase materials: x = 0 – 0.6 — sp. gr. *R*3*C*, x = 0.8 – sp. gr. *Imma*, x = 1 — sp. gr. *Pnma*	103
$BaCe_{0.80}Gd_{0.2-x}Pr_xO_{3-\delta}$ (x = 0.005, 0.01, 0.015, 0.02, 0.05, 0.1)	Solid-state reaction	1350	10	Orthorhombic structure	104
$Ba(Ce_{0.8-x}Pr_xGd_{0.2})O_{3-\delta}$ (x = 0.4, 0.6, 0.8)	Solid-state reaction	–	–	Orthorhombic (sp. gr. *Pmcn*)	105
$BaZr_{0.85}Y_{0.1}Pr_{0.05}O_{3-\delta}$	Solid-state reaction	1400	32	Cubic structure	76
$BaCe_{0.8}Pr_{0.2}O_{3-\delta}$	Solid-state reaction	1250	10	Orthorhombic structure	106
$BaZr_{0.8-x}Pr_xY_{0.2}O_{3-\delta}$ (x = 0 – 0.4)	Combustion synthesis procedure	1100	6	Single phase	107
$BaZr_{0.9-x}Pr_{0.1}Y_xO_{3-\delta}$ (x = 0, 0.1, 0.2)	Combustion method	1100	6	Cubic structure	108

For the $BaZr_{1-x}Fe_xO_{3-\delta}$ system, a difference in ionic radii is considerably lower ($r^{VI}_{Zn^{4+}}$ = 0.72 Å), leading to the appearance of solid solutions in the wider concentration range: $0 \leqslant x \leqslant 0.6$ [54] or $0 \leqslant x \leqslant 0.4$.[78]

In general, the Co-doped cerates and zirconates display the same phase behaviour due to the closely related nature of Co-ions to Fe-ions. For example, $BaCe_{1-x}Co_xO_{3-\delta}$ and $BaZr_{1-x}Co_xO_{3-\delta}$ are single-phase at $0 \leqslant x \leqslant 0.1$ [77] or $0 \leqslant x \leqslant 0.4$,[101] respectively.

A different tendency is observed for the Pr-doped $Ba(Ce,Zr,R)O_3$, where solid solutions can be formed over the entire concentration range.[38, 103] This might additionally be explained in terms of the relatively close ionic radii (for cerates, $r^{VI}_{Pr^{4+}} = 0.85$ Å). Moreover, praseodymium has similar chemical properties to cerium, allowing the formation of a $BaPrO_3$-based system with proton transportation.

3.2. Chemical compatibility with the proton-conducting electrolytes

The chemical compatibility of the functional materials used together at elevated temperatures is an important property for ensuring high-performance characteristics and the stability over long periods of time. It is well known that the long-term operation of SOFCs can result in the interdiffusion of cations; as a result, impurity- (and, as a rule, low conductive or ionic-blocking) phases are formed at the interface.[109 – 112] In order to overcome this drawback, various strategies can be utilised.

One of the most rational approaches concerns a decrease in the maximal temperatures of cathode fabrication and SOFC operation down to the low-temperature range.[26, 113, 114] This leads to a considerable improvement in the quality of the interface due to a reduced chemical interaction rate. However, the electrochemical performance of the functional materials can be unsatisfactory due to the high ohmic resistance of the electrolyte and slow electrochemical kinetics of the electrodes.

Another strategy lies in the utilisation of buffer layers, which prevent the formation of contact phases between chemically active compounds. A vivid confirmation of this can be seen in the porous cerium-based buffer layers ($Ce_{1-x}R_xO_{2-\delta}$, where R = Y, Gd, Sm or La, $0.1 \leqslant x \leqslant 0.3$) placed between the conventional YSZ electrolyte and LSM as La-based electrodes. Here, YSZ is the yttria-stabilised zirconia, $Zr_{1-x}Y_xO_{2-\delta}$; LSM is the lanthanum strontium manganite, $La_{1-x}Sr_xMnO_{3-\delta}$. This additional layer prevents the formation of a $La_2Zr_2O_7$-insulator phase at the interface due to a lack of direct contact between YSZ and LSM.[115 – 117] However, even in this case a chemical interaction is possible, since cationic interdiffusion between LSM, YSZ and doped CeO_2 over a long period of time might also lead to the formation of $SrCeO_3$ or $SrZrO_3$ exhibiting low ionic conductivities.[118 – 120]

As can be seen from the provided examples, the arising problems are associated with the strong chemical differences between the functional materials, on the one hand, and the ability to form wide ranges of solid solutions and new compounds, on the other hand. It is evident that these problems can be partially or fully eliminated by designing electrolyte/electrode pairs composed of the same fragmentary type. In that case, as mentioned above, their chemical activity will be determined by nature of the dopants [R and M in M-doped $Ba(Ce,Zr,R)O_3$ electrodes and R-doped $Ba(Ce,Zr)O_3$ electrolytes]. An analysis of experimental results (Table 2) shows that these phases are definitely compatible.

3.3. Thermo-mechanical and chemo-mechanical behaviour

Issues associated with mechanical compatibility of the functional materials used together in electrochemical cells are more complex in the case of protonic-conducting systems compared with their oxygen-conducting analogues. This is due to the fact that the thermo-chemical behaviour of the PCFC or its components depends not only on two external parameters (temperature and oxygen partial pressure), but also on water vapour partial pressure, resulting in a wide variation of strain effects, as illustrated in Fig. 6 *a*. In case of the materials having different responses to changes in T, p_{O_2} and p_{H_2O}, the mechanical stresses between them can increase to such a degree that irreversible processes (layer delamination, cracks or pore formation, see Fig. 4) can result in the destruction of the entire electrochemical system.

Materials considered for high-temperature application can be divided in three main groups (Fig. 6 *a*):

1. Oxides whose thermal expansion behaviour depends mainly on the temperature factor. This group includes materials composed of cations having a constant oxidation state — for example, YSZ [124, 125] — as well as single-phase materials based on transition elements, which exhibit a slight variation in terms of oxygen stoichiometry ($La_{1-x}Sr_xMnO_{3-\delta}$, $Ln_2NiO_{4+\delta}$, $LaNi_{0.6}Fe_{0.4}O_{3-\delta}$) depending on p_{O_2} at higher temperatures.[124, 126, 127]

2. Oxides showing a p_{O_2}-induced chemical strain along with conventional thermal strain. Such mixed behaviour occurs for materials composed of transition elements, whose oxidation and spin states can be quite easily altered with p_{O_2}

Table 2. High chemical compatibility (no interaction) of R-doped electrolyte and M-doped electrode materials revealed for calcined mixtures on the basis of X-ray diffraction analysis: R = Y and/or Yb, M = Co and/or Fe.

Electrolyte composition	Electrode composition	Weight ratio	Calcination parameters		Ref.
			T/°C	τ/h	
$BaZr_{0.1}Ce_{0.7}Y_{0.1}Yb_{0.1}O_{3-\delta}$	$BaFe_{0.6}Co_{0.3}Ce_{0.1}O_{3-\delta}$	1 : 2	1100	3	85
$BaZr_{0.1}Ce_{0.7}Y_{0.2}O_{3-\delta}$	$BaZr_{0.1}Ce_{0.7}Co_{0.2}O_{3-\delta}$	—	—	—	97
$BaZr_{0.1}Ce_{0.7}Y_{0.2}O_{3-\delta}$	$BaCe_{0.5}Fe_{0.3}Bi_{0.2}O_{3-\delta}$	1 : 1	950	3	83
$BaZr_{0.1}Ce_{0.7}Y_{0.2}O_{3-\delta}$	$Ba_{0.9}Co_{0.4}Fe_{0.4}Zr_{0.1}Y_{0.1}O_{3-\delta}$	1 : 1	1200	10	87
$BaCe_{0.7}Zr_{0.1}Y_{0.1}Yb_{0.1}O_{3-\delta}$	$BaCo_{0.4}Fe_{0.4}Zr_{0.1}Y_{0.1}O_{3-\delta}$	3 : 2	1100	4	121
$BaZr_{0.1}Ce_{0.7}Y_{0.1}Yb_{0.1}O_{3-\delta}$	$BaCo_{0.7}(Ce_{0.8}Y_{0.2})_{0.3}O_{3-\delta}$	1 : 1	1000	2	100
$BaCe_{0.7}Zr_{0.1}Y_{0.1}Yb_{0.1}O_{3-\delta}$	$BaCo_{0.4}Fe_{0.4}Zr_{0.2}O_{3-\delta}$	1 : 1	1000	9	94

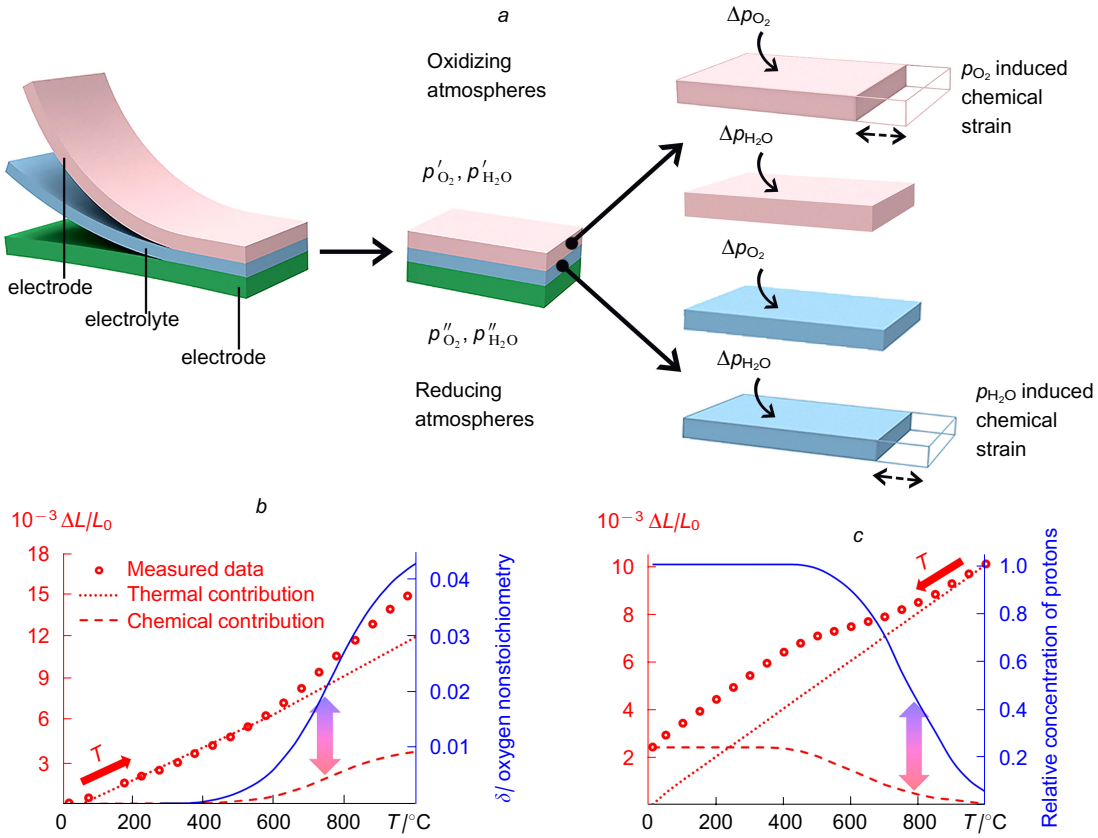


Figure 6. Thermo-chemical behaviour of functional materials: (*a*) basic representation of solid oxide electrochemical cells based on proton-conducting electrolytes and linear response of the functional materials towards p_{O_2} and p_{H_2O} variations; dilatometric curves of $Ce_{0.9}Pr_{0.1}O_{2-\delta}$ (*b*) and $BaCe_{0.8}Y_{0.2}O_{3-\delta}$ (*c*) measured under ambient conditions. The data of panel (*b*) are adopted from Ref. 122, while the data of panel (*c*) are taken from Ref. 123. $\Delta L/L_0$ is the relative change of linear parameters.

variation, for example, $Ce_{1-x}Pr_xO_{2-\delta}$, $SrFe_{1-x}Ti_xO_{3-\delta}$ and $LnBaCo_2O_{5+\delta}$.[128–130]

3. Oxides having a pronounced p_{H_2O}-induced chemical strain as a result of their hydration/dehydration. The most widely known representatives of this group are cerates and zirconates of alkaline-earth elements.[123, 131–133]

The mechanistic nature of p_{O_2}-induced chemical strain for oxide materials is thoroughly described in the review works of Bishop *et al.*[134] and Herklotz *et al.*[135] In brief, this effect appears to be caused by changes in the chemical composition of an oxide, particularly its oxygen stoichiometry, δ. In turn, the δ variation affects the concentration of point defects due to their interaction (see, for example, Eqs. 7 and 8). Respectively, the reference conditions, the appearance of oxygen vacancies at the anionic sublattice and the reduction of cations at the cationic positions are dimension-determined processes, which can either play an individual role (under isothermal conditions) or take place along with thermal strain, see Fig. 6 *b*.

p_{H_2O}-Induced chemical strain affects lattice deformation upon water uptake (Eqn 3), when the oxygen atom of a water molecule fills a vacant position in the anionic sublattice.[53] From a macroscopic point of view, this process leads to an increase in the effective ionic radius of the oxygen site ($r_{V_O^{\bullet\bullet}} = 1.18$ Å, $r_{OH_O^{\bullet}} = 1.35$ Å)[133,136] and, accordingly, its dimensional parameters. For example, a decrease in temperature in a humid atmosphere leads to a decrease in the relative change of linear dimensions for an almost completely dehydrated proton-conducting material (that does not undergo phase transitions), as illustrated in Fig. 6 *c*. Under conditions of relatively high temperatures, at which the hydration effect is negligible, this decrease is mainly associated with the thermal effect. At lower temperatures, the oxide starts to take up water in accordance with Reaction 3, chemically expanding in view of the mentioned differences in effective ionic radii. As a result, the experimental dependence deviates from linearity; in this case, the dilatometric curve has a bend, which is not associated with a phase transition (for example, doped $BaZrO_3$). However, the nature of the dilatometric curve becomes more complicated in the case of a polymorphic material, whose crystal structure can be determined not only by temperature, but also by p_{H_2O} (for example, doped $BaCeO_3$).

In concluding the discussion regarding chemical strain features, we should stress that proton-conducting electrolytes, which have high mechanical tolerance towards changes in p_{O_2}, are sensitive to p_{H_2O} changes in a gas phase. On the other hand, the dimension parameters of complex oxides serving as electrodes are determined by the p_{O_2} variation with a small (or negligible) response to the p_{H_2O} change. It is evident that chemical strain incompatibility is a serious issue in terms of the real application of electrochemical cells based on $Ba(Ce,Zr)O_3$ electrolytes. This issue should be thoroughly considered at the fabrication and operation stages of the corresponding cells and stacks.[137] The thermal expansion coefficient (TEC, α) is a convenient parameter for use in the qualitative analysis of material compatibility. This coefficient is usually deter-

mined within a certain range of temperatures, when dilatometry dependences are close to the linear form. On the basis of the presented cases (Fig. 6 *b* and *c*), 'pure' TECs calculated for the thermal part of the overall expansion achieve around 12.7×10^{-6} and 10.2×10^{-6} K^{-1} for $Ce_{0.9}Pr_{0.1}O_{2-\delta}$ and $BaCe_{0.8}Y_{0.2}O_{3-\delta}$, respectively. However, for real (measured) data, various TECs values are observed. For example, the dilatometric curve of $Ce_{0.9}Pr_{0.1}O_{2-\delta}$ is not linear across the whole temperature range: two linear regions can be distinguished, 20–570 and 570–970 °C, with the corresponding TECs of 11.2×10^{-6} and 21.9×10^{-6} K^{-1}, respectively. The same phenomenon occurs for the second case ($BaCe_{0.8}Y_{0.2}O_{3-\delta}$), when three close-to-line regions take place at 20–350, 350–800 and 800–1000 °C with corresponding TECs of 10.2×10^{-6}, 5.2×10^{-6} and 8.1×10^{-6} K^{-1}, respectively. Such measured parameters are called apparent TECs, since they correspond to a mixed (thermal and chemical) strain effects instead of solely thermal ones.

Problems in thermo-chemical compatibility consist not only in different TECs calculated for the same materials across both low- and high-temperature ranges, but also in the fact that different materials possess unequal TEC values within the same temperature range. To reduce possible thermal stresses, PCFC and PCEC functional materials should exhibit similar thermo-chemical behaviour. The creation of electrolytes and electrodes composed of similar structural fragments (barium at the A-site and cerium/zirconium at the B-site of a ABO_3 perovskite) is one of the possible ways of solving the above mentioned problems. However, even in this case, the TEC discrepancy can be considerable. As shown in Fig. 7 *a*,*b*, the average TECs rise with an increase of M concentration in the M-doped $Ba(Ce,Zr)O_3$ systems: from $8-10\times10^{-6}$ K^{-1} for $Ba(Ce,Zr,Ln)O_3$ oxides to 25×10^{-6} K^{-1} for their heavy M-doped counterparts. As mentioned above, extremely high TECs result from the p_{O_2}-chemical induced strain occurring for materials based on the transition elements (see Eqs. 7 and 8).

By frequently comparing in use electrode systems based on cobalt (cobaltites) and iron (ferrites), it can be concluded that the cobalt concentration should be minimised, since it results in very high TEC levels (Fig. 7 *c*). Nevertheless, at the same time, the TEC differences calculated within different temperature regions can be reduced. The provided example is in line with the currently promising strategy in materials science; according to this, a rational design in oxygen (steam) electrodes of PCFCs/PCECs is associated with Co-free materials having decreased thermo-chemical strain.[138, 140–146]

When comparing the mechanical compatibility of R-doped $Ba(Ce,Zr)O_3$ and M-doped $Ba(Ce,Zr,R)O_3$, it is clear that priority in electrode design should be given to systems with a low-to-medium concentration of the M-transition elements. Otherwise, apparent TECs reach high levels for the extreme members of M-doped $Ba(Ce,Zr,R)O_3$: $\sim24\times10^{-6}$ K^{-1} (800–1100 °C) for $BaFeO_3$[147] and $\sim24\times10^{-6}$ K^{-1} (25–900 °C) for $BaCoO_3$.[148]

3.4. Hydration capability

Information concerning the water uptake of complex oxides is of special interest in terms of the possibility to design triple-conducting materials[149] with the most attractive electrochemical activity in PCFCs/PCECs (see Fig. 5 *c*). Although this belongs to a mainstream area,[24, 68, 69, 150–153] there is a limited number of indisputable evidences of meaningful proton transportation in single-phase electrode materials based on simple or double perovskite structures.[154, 155] The main difficulty in analysing proton conductivity (in oxides with very high contributions of oxygen-ionic and electronic conductivities) consists in the fact that the water uptake occupies an intermediate position between the water absorption of material surfaces and the strong interaction between them followed by oxide decomposition and hydroxide formation. Correspondingly, many convenient techniques used for the determination of proton conductivity in the conventional proton-conducting materials [such as thermogravimetric (TG) measurements in dry *vs.*

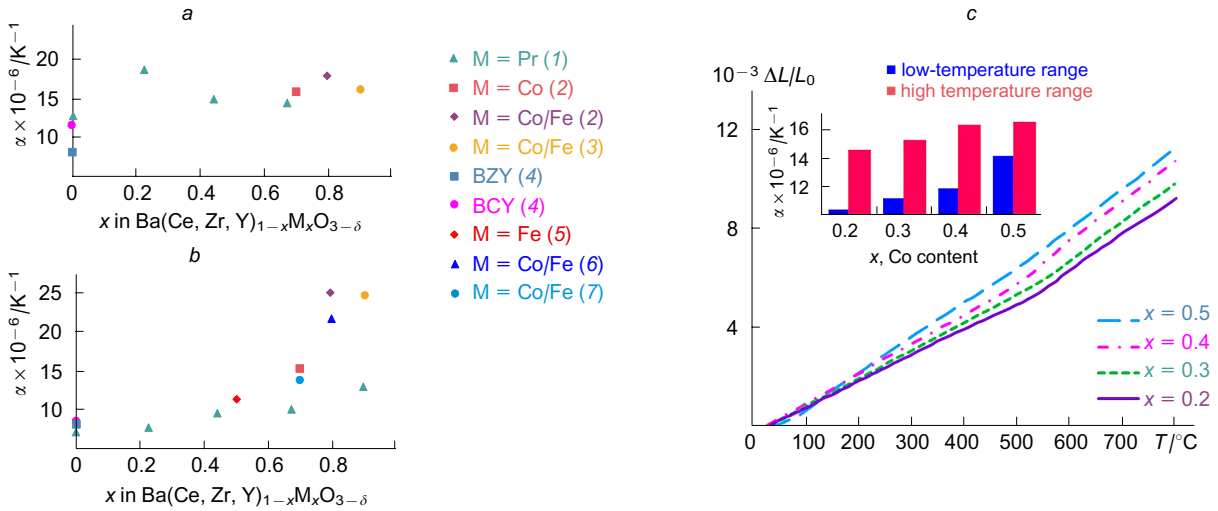


Figure 7. Thermal expansion coefficients (α) of $Ba(Ce,Zr,Y)_{1-x}M_xO_{3-\delta}$ materials as a function of M-content (x) in low-temperature (*a*) and high-temperature (*b*) ranges, where: (*1*) $Ba(Zr_{0.7}Ce_{0.2})_{1-x/0.9}Pr_xY_{0.1}O_{3-\delta}$,[38] (*2*) $BaCo_{0.4}Fe_{0.4}Zr_{0.1}Y_{0.1}O_{3-\delta}$ and $BaCo_{0.7}(Ce_{0.8}Y_{0.2})_{0.3}O_{3-\delta}$,[100] (*3*) $BaFe_{0.6}Ce_{0.1}Co_{0.3}O_{3-\delta}$,[91] (*4*) $BaZr_{0.8}Y_{0.2}O_{3-\delta}$ and $BaCe_{0.8}Y_{0.2}O_{3-\delta}$,[138] (*5*) $BaCe_{0.5}Fe_{0.5}O_{3-\delta}$,[83] (*6*) $BaCo_{0.4}Fe_{0.4}Zr_{0.2}O_{3-\delta}$,[139] (*7*) $BaFe_{0.7-x}Co_xZr_{0.3}O_{3-\delta}$ samples.[90] Thermal expansion curves and concentration dependences of TECs for the $BaFe_{0.7-x}Co_xZr_{0.3}O_{3-\delta}$ ceramic samples (*c*).[90]

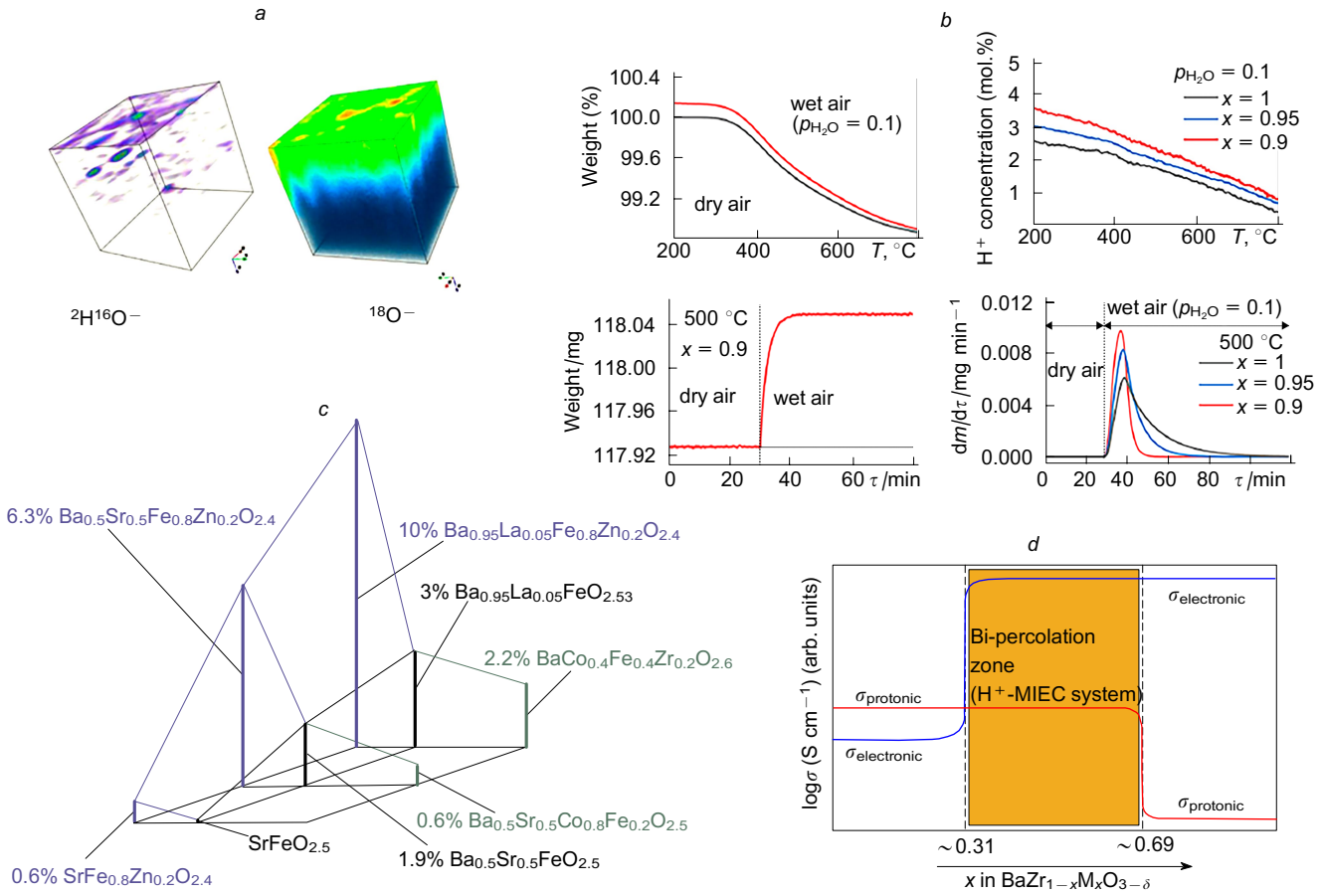


Figure 8. Water uptake properties of Co- and Fe-containing electrode materials: (*a*) false colour 3D maps of the $^2H^{16}O^-$ and $^{18}O^-$ ion intensities of the analysed area for the $PrBaCo_2O_{5+\delta}$ sample;[154] (*b*) TG results obtained for the $Ba_xCo_{0.4}Fe_{0.4}Zr_{0.2}O_{3-\delta}$ compounds at different conditions;[89] (*c*) mole proton concentration of perovskite-related oxides at 250 °C and p_{H_2O} ~ 0.016;[168] (*d*) partial conductivities protons and holes in the M-doped $BaZrO_3$ system.[52]

wet conditions, separation of conductivity on the basis of its profile depending on p_{O_2} or p_{H_2O}][156–159] cannot be employed to determine the proton conductivity of triple-conducting oxides.

Kim *et al.*[68] first postulated the triple-conducting behaviour of a $NdBa_{0.5}Sr_{0.5}Co_{1.5}Fe_{0.5}O_{5+\delta}$ phase, initiating active research efforts. As a result, different double perovskite materials (such as $NdBaCo_{2-x}Mn_xO_{5+\delta}$,[160] $GdBaCo_2O_{5+\delta}$,[161] $PrBa_{0.5}Sr_{0.5}Co_{1.5}Fe_{0.5}O_{5+\delta}$)[162] have been proposed as possible candidates having a proton transfer sign. However, Lozano *et al.*,[154] using isotopic exchange studies in a system of $PrBaCo_2O_{5+\delta}$ (PBC) with $^{18}O_2$ and $^2H_2{}^{16}O$ at elevated temperatures, have revealed that no visible water uptake can be attributed to the bulk properties of PBC; instead, only hydrogen is localised at the large-scale, near-surface defect regions (pores or BaO-enriched phases, see Fig. 8 *a*).

From a general viewpoint, it is clear that a high quantity of protons can be realised for cathode materials having fragments of a similar structure using conventional proton-conducting electrolytes. Taking this into account, Shang *et al.*[86] have proposed a new composition of $BaCo_{0.4}Fe_{0.4}Zr_{0.2}O_{3-\delta}$ (BCFZ) designed from a well-known $BaZrO_3$ matrix phase co-doped with cobalt and iron. Although basicity (responsible for high proton uptake of doped zirconates/cerates) deteriorates with the introduction of Co/Fe, high quantities of such elements do not prohibit water uptake for the obtained derivatives.[163, 164] According to Zohourian *et al.*,[92] the proton concentration of BCFZ reaches 1.5% and 0.5% at 200 and 400 °C, respectively, when p_{H_2O} is equal to ~0.016 (estimated conductivity level reaches 0.09 – 0.3 mS cm^{-1} at 350 – 600 °C).[165] The concentration levels were calculated using the BCFZ defect structure as well as TG data in dry and wet conditions. Ren *et al.*[89] also proposed a strategy for improving proton transport of BCFZ. They found that a Ba-deficiency in $Ba_xCo_{0.4}Fe_{0.4}Zr_{0.2}O_{3-\delta}$ (x = 0.90, 0.95 and 1.00) increases the achievable hydration, leading to an increase by 40% – 100% in proton concentration, Fig. 8 *b*. The proton transportation of the Y-doped BCFZ ($BaCo_{0.4}Fe_{0.4}Zr_{0.1}Y_{0.1}O_{3-\delta}$, BCFZY) was confirmed by Chen *et al.* utilising an electrical conductivity relaxation technique.[166] It should be mentioned that both BCFZ and BCFZY electrode compositions have been successfully used by the O'Hayre research group to fabricate PCFCs/PCECs that demonstrate outstanding performance.[88, 139, 167]

Recently, Zohourian *et al.*[168] revealed a relation between proton concentration of the perovskite-structured oxides (ABO_3) and their crystallochemical factors (ion basicity, B-site cations and their oxidation state and B – O covalency), which can be illustrated in Fig. 8 *c*. According to the performed experiments, $Ba_{0.95}La_{0.05}Fe_{0.8}Zn_{0.2}O_{3-\delta}$ exhibits the highest proton concentration among ~20 studied materials, exceeding ~5 times that of BCFZ under the same

conditions. Despite this fact, BCFZ and BCFZY have been more widely studied than $Ba_{0.95}La_{0.05}Fe_{0.8}Zn_{0.2}O_{3-\delta}$ (Refs 87, 90, 93, 166, 169 and 170). Kim *et al.*[52] explained the rather low proton conductivity levels for the heavy M-doped barium cerates or zirconates in terms of percolation theory (Fig. 8 *d*).

Proton transfer is indirectly proposed as being realised for such oxide materials whose electrochemical activity improves with air humidification. This comes from the standard interpretation of the following equation

$$R_p \propto (p_{O_2})^{-n}(p_{H_2O})^{-m} \quad (14)$$

Here, R_p is the polarisation resistance of the electrodes, n and m are the power functions varying from 0 to 1 and the determining mechanism of the electrode processes.[171 – 173] Although this assumption needs more detailed confirmation, the polarisation resistance of many oxide materials might decrease with an increase in p_{H_2O} in oxidising atmospheres, including $Ln_2NiO_{4+\delta}$ phases,[174, 175] layered oxides $Ca_3Co_4O_{9+\delta}$ and $Sr_3Fe_2O_{7-\delta}$,[145, 176] and perovskite-related materials of $Ba_{0.5}Sr_{0.5}Co_{0.8}Fe_{0.2}O_{3-\delta}$,[177, 178] $SrSc_{0.175}Nb_{0.025}Co_{0.8}O_{3-\delta}$,[70] and $PrBaCo_{2-x}Fe_xO_{5+\delta}$.[179] This is a useful property in terms of their application under highly humid conditions (realised, for example, in SOECs).

3.5. Electrical conductivity

The electrode materials should have a suitable (high) level of electronic conductivity to provide good electrical connection between the electrolyte/electrode interface region and the current collectors of the external electrical circuit.[180] Typically, this level needs to be higher than 100 S cm^{-1} in a dense form, since for a porous state it decreases by more than one order of magnitude compared to the dense state according to the two-phase material percolation theory, when gas in pores represents one (insulating) of the phases (see Bruggeman asymmetric model described in detail in Refs 181 – 183). Table 3 provides a comparative analysis of electrical properties for cerates/zirconates doped with cobalt, iron or praseodymium as transition elements, while Fig. 9 repeats these data for clarity of presentation.

Table 3. Electrical conductivity of M-doped Ba(Ce,Zr)O_3-based materials measured by 4-probe direct current method in ambient air atmosphere.

Composition	M	x /content of M	σ /S cm^{-1}		Ref.
			600 °C	700 °C	
$BaZr_{0.1}Ce_{0.7}Y_{0.18}Co_{0.02}O_{3-\delta}$	Co	0.02	8.0×10^{-3}	1.8×10^{-2}	97
$BaZr_{0.1}Ce_{0.7}Y_{0.15}Co_{0.05}O_{3-\delta}$	Co	0.05	3.0×10^{-3}	9.0×10^{-3}	97
$BaCe_{0.85}Y_{0.1}Co_{0.05}O_{3-\delta}$	Co	0.05	6.4×10^{-3}	8.9×10^{-3}	56
$BaCe_{0.825}Y_{0.1}Co_{0.075}O_{3-\delta}$	Co	0.075	6.4×10^{-3}	8.9×10^{-3}	56
$BaCe_{0.85}Co_{0.05}Y_{0.1}O_{3-\delta}$	Co	0.05	3.5×10^{-3}	5.8×10^{-3}	98
$BaCe_{0.82}Co_{0.08}Y_{0.1}O_{3-\delta}$	Co	0.08	1.6×10^{-3}	3.7×10^{-3}	98
$BaCe_{0.8}Co_{0.1}Y_{0.1}O_{3-\delta}$	Co	0.1	2.3×10^{-3}	5.1×10^{-3}	98
$BaZr_{0.1}Ce_{0.7}Y_{0.1}Co_{0.1}O_{3-\delta}$	Co	0.1	8.8×10^{-2}	1.7×10^{-1}	97
$BaZr_{0.1}Ce_{0.7}Y_{0.1}Co_{0.1}O_{3-\delta}$	Co	0.1	1.5×10^{-3}	3.4×10^{-3}	77
$BaCe_{0.8}Y_{0.1}Co_{0.1}O_{3-\delta}$	Co	0.1	5.6×10^{-3}	7.8×10^{-3}	56
$BaZr_{0.9}Co_{0.1}O_{3-\delta}$	Co	0.1	4.4×10^{-2}	5.7×10^{-2}	101
$BaZr_{0.1}Ce_{0.7}Co_{0.2}O_{3-\delta}$	Co	0.2	2.0	2.6	97
$BaCe_{0.7}Co_{0.2}Y_{0.1}O_{3-\delta}$	Co	0.2	1.8×10^{-2}	3.4×10^{-2}	98
$BaZr_{0.8}Co_{0.2}O_{3-\delta}$	Co	0.2	1.6×10^{-1}	1.8×10^{-1}	77
$BaZr_{0.7}Co_{0.3}O_{3-\delta}$	Co	0.3	2.0×10^{-1}	2.1×10^{-1}	77
$BaZr_{0.6}Co_{0.4}O_{3-\delta}$	Co	0.4	2.4×10^{-1}	2.6×10^{-1}	52
$BaZr_{0.5}Co_{0.5}O_{3-\delta}$	Co	0.5	3.0×10^{-1}	3.1×10^{-1}	77
$BaCo_{0.7}(Ce_{0.8}Y_{0.2})_{0.3}O_{3-\delta}$	Co	0.7	2.5	3.2	100
$BaZr_{0.85}Y_{0.1}Fe_{0.05}O_{3-\delta}$	Fe	0.05	1.0×10^{-3}	2.0×10^{-3}	76
$BaCe_{0.85}Y_{0.1}Fe_{0.05}O_{3-\delta}$	Fe	0.05	3.8×10^{-3}	$5.0\ 10^{-3}$	56
$BaCe_{0.825}Y_{0.1}Fe_{0.075}O_{3-\delta}$	Fe	0.075	3.7×10^{-3}	4.9×10^{-3}	56
$BaZr_{0.1}Ce_{0.7}Y_{0.1}Fe_{0.1}O_{3-\delta}$	Fe	0.1	5.9×10^{-4}	1.3×10^{-3}	77
$BaZr_{0.9}Fe_{0.1}O_{3-\delta}$	Fe	0.1	1.5×10^{-4}	9.9×10^{-4}	52
$BaZr_{0.8}Fe_{0.2}O_{3-\delta}$	Fe	0.2	1.7×10^{-3}	3.7×10^{-4}	52
$BaZr_{0.67}Fe_{0.33}O_{3-\delta}$	Fe	0.33	4.7×10^{-2}	2.6×10^{-2}	52
$BaCe_{0.4}Sm_{0.2}Fe_{0.4}O_{3-\delta}$	Fe	0.4	2.8×10^{-2}	3.6×10^{-2}	71

Table 3 (continued).

Composition	M	x /content of M	σ /S cm^{-1}		Ref.
			600 °C	700 °C	
$BaCe_{0.4}Sm_{0.2}Fe_{0.4}O_{3-\delta}$	Fe	0.4	2.4×10^{-2}	3.0×10^{-2}	72
$BaCe_{0.5}Fe_{0.5}O_{3-\delta}$	Fe	0.5	9.4×10^{-1}	7.8×10^{-1}	74
$BaZr_{0.5}Fe_{0.5}O_{3-\delta}$	Fe	0.5	8.7×10^{-4}	1.2×10^{-3}	78
$BaFe_{0.6}Ce_{0.1}Co_{0.3}O_{3-\delta}$	Fe	0.6	1.8	1.5	91
$BaCo_{0.7}Fe_{0.2}Zr_{0.1}O_{3-\delta}$	Fe/Co	0.9	8.5	8.2	95
$BaCo_{0.7}Fe_{0.24}Zr_{0.06}O_{3-\delta}$	Fe/Co	0.94	10.3	9.0	95
$BaCo_{0.2}Fe_{0.5}Zr_{0.3}O_{3-\delta}$	Fe/Co	0.7	1.0	1.1	90
$BaCo_{0.3}Fe_{0.4}Zr_{0.3}O_{3-\delta}$	Fe/Co	0.7	1.6	1.7	90
$BaCo_{0.4}Fe_{0.3}Zr_{0.3}O_{3-\delta}$	Fe/Co	0.7	1.9	2.3	90
$BaCo_{0.5}Fe_{0.2}Zr_{0.3}O_{3-\delta}$	Fe/Co	0.7	4.1	4.9	90
$BaCo_{0.4}Fe_{0.4}Zr_{0.1}Y_{0.1}O_{3-\delta}$	Fe/Co	0.8	1.4	–	88
$BaCo_{0.4}Fe_{0.4}Zr_{0.1}Y_{0.1}O_{3-\delta}$	Fe/Co	0.8	1.2	1.3	100
$BaZr_{0.85}Y_{0.1}Pr_{0.05}O_{3-\delta}$	Pr	0.05	6.0×10^{-3}	1.0×10^{-2}	76
$BaZr_{0.7}Pr_{0.1}Y_{0.2}O_{3-\delta}$	Pr	0.1	1.2×10^{-2}	1.8×10^{-2}	107
$BaZr_{0.7}Pr_{0.1}Y_{0.2}O_{3-\delta}$	Pr	0.1	1.2×10^{-2}	2.5×10^{-2}	108
$BaCe_{0.85}Pr_{0.15}O_{3-\delta}$	Pr	0.15	1.1×10^{-4}	2.6×10^{-4}	184
$BaCe_{0.85}Pr_{0.15}O_{3-\delta}$	Pr	0.15	1.3×10^{-4}	3.1×10^{-4}	185
$BaZr_{0.49}Ce_{0.14}Pr_{0.2}Y_{0.1}O_{3-\delta}$	Pr	0.2	2.0×10^{-3}	7.0×10^{-3}	103
$BaCe_{0.8}Pr_{0.2}O_{3-\delta}$	Pr	0.2	2.2×10^{-3}	1.3×10^{-3}	106
$BaZr_{0.6}Pr_{0.2}Y_{0.2}O_{3-\delta}$	Pr	0.2	1.4×10^{-2}	2.0×10^{-2}	107
$BaZr_{0.525}Ce_{0.15}Pr_{0.225}Y_{0.1}O_{3-\delta}$	Pr	0.225	8.0×10^{-3}	2.2×10^{-2}	38
$BaZr_{0.5}Pr_{0.3}Y_{0.2}O_{3-\delta}$	Pr	0.3	1.6×10^{-2}	2.1×10^{-2}	107
$BaZr_{0.35}Ce_{0.1}Pr_{0.4}Y_{0.1}O_{3-\delta}$	Pr	0.4	2.0×10^{-2}	3.9×10^{-2}	103
$BaCe_{0.4}Pr_{0.4}Gd_{0.2}O_{2.9}$	Pr	0.4	8.9×10^{-2}	1.1×10^{-1}	105
$BaZr_{0.4}Pr_{0.4}Y_{0.2}O_{3-\delta}$	Pr	0.4	2.8×10^{-2}	4.0×10^{-2}	107
$BaZr_{0.354}Ce_{0.101}Pr_{0.445}Y_{0.1}O_{3-\delta}$	Pr	0.445	3.7×10^{-2}	7.1×10^{-2}	38
$BaZr_{0.21}Ce_{0.06}Pr_{0.6}Y_{0.1}O_{3-\delta}$	Pr	0.6	1.1×10^{-1}	1.9×10^{-1}	103
$BaCe_{0.2}Pr_{0.6}Gd_{0.2}O_{3-\delta}$	Pr	0.6	1.2×10^{-1}	1.3×10^{-1}	105
$BaZr_{0.175}Ce_{0.05}Pr_{0.675}Y_{0.1}O_{3-\delta}$	Pr	0.675	1.1×10^{-1}	2.0×10^{-1}	38
$BaZr_{0.07}Ce_{0.02}Pr_{0.8}Y_{0.1}O_{3-\delta}$	Pr	0.8	2.0×10^{-1}	2.9×10^{-1}	103

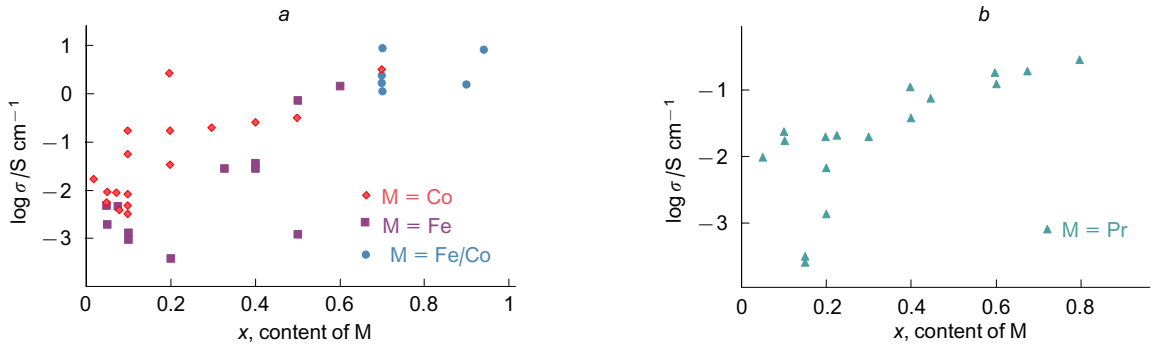


Figure 9. Electrical conductivity of M-doped $Ba(Ce,Zr)O_3$ materials at 700 °C depending on the type of M and its concentration: M = Co and/or Fe (*a*) and Pr (*b*). These data are taken from Table 3.

It can be seen that for the Co- and Fe-doped systems, there is a wide window of conductivity noise (Fig. 9 *a*) that can depend on many factors, including phase inhomogeneity (single-phase materials, two-phase materials, secondary phases), the different porosity (or relative density) of the samples, different charge conditions of Co- or Fe-ions. However, the obvious tendency towards an improvement in conductivity is observed at higher quantities of these cations, qualitatively satisfying the tendency mentioned in Fig. 9 *b*. Nevertheless, none of the considered examples show an electronic conductivity higher than 10 S cm^{-1} (level of nominally pure $BaFeO_3$ is about 5 S cm^{-1} at 500 °C);[186] as a result, the real conductivity level of porous electrodes produced using these compositions is estimated at not more than 1 S cm^{-1}, which fails to provide excellent current distribution. This fact is not discussed in the literature in terms of the applicability of M-doped Ba(Ce,Zr)O_3 electrodes in PCFCs/PCECs. Therefore, it is difficult to reach current densities as high as 2 – 4 A cm^{-2}.[87, 93, 187] A well-developed microstructure of the electrodes as well as the use of the electro(catalytical) additives or current collectors might improve current distribution in a case of the M-doped Ba(Ce,Zr)O_3 electrodes with an insufficient electronic conductivity.

Analysis of the Pr-doped systems shows that the conductivity of the designed samples is less than 1 S cm^{-1} for the heavy-doped examples. This fact does not permit their application as electrodes in PCFCs/PCECs.

4. Performance of the M-doped Ba(Ce,Zr)O_3 electrodes

This Section presents evaluation of the $BaCeO_3$- or $BaZrO_3$-based materials doped with cobalt and iron (as the most frequently used dopants) from the viewpoint of their application in electrochemical devices. First, electrochemical

Table 4. Possible elementary stages for a couple of proton-conducting electrolyte with an electrode having electronic, oxygen-ionic/electronic or triple-conducting behaviour (presented for fuel cell operation mode).

No.	e′ conductors	O^{2-}/e′ conductors	H^+/O^{2-}/e′ conductors
		Oxygen path	
1.1	$O_{2\ gas} \rightleftarrows O_{2\ ads,\ ed}$	$O_{2\ gas} \rightleftarrows O_{2\ ads,\ ed}$	$O_{2\ gas} \rightleftarrows O_{2\ ads,\ ed}$
1.2	$O_{2\ ads,\ ed} \rightleftarrows 2\,O_{ads,\ ed}$	$O_{2\ ads,\ ed} \rightleftarrows 2\,O_{ads,\ ed}$	$O_{2\ ads,\ ed} \rightleftarrows 2\,O_{ads,\ ed}$
1.3	$O_{ads,\ ed} \rightleftarrows O_{TPB,\ ed}$	$O_{ads,\ ed} \rightleftarrows O_{TPB,\ ed}$	$O_{ads,\ ed} \rightleftarrows O_{(TPB,\ ed}$
1.4	$O_{ads,\ ed} + 2\,e'_{surf,\ ed} \rightleftarrows O^{2-}_{ads,ed}$	$O_{ads,\ ed} + 2\,e'_{surf,\ ed} \rightleftarrows O^{2-}_{ads,ed}$	$O_{ads,\ ed} + 2\,e'_{surf,\ ed} \rightleftarrows O^{2-}_{ads,ed}$
1.5	$O^{2-}_{ads,ed} \rightleftarrows O^{2-}_{TPB,ed}$	$O^{2-}_{ads,ed} \rightleftarrows O^{2-}_{TPB,ed}$	$O^{2-}_{ads,ed} \rightleftarrows O^{2-}_{TPB,ed}$
1.6		$O_{ads,\ ed} + 2\,e'_{surf,\ ed} \rightleftarrows O^{2-}_{ads,ed}$	$O_{ads,\ ed} + 2\,e'_{surf,\ ed} \rightleftarrows O^{2-}_{ads,ed}$
1.7		$O^{2-}_{ads,ed} \rightleftarrows O^{2-}_{bulk,ed}$	$O^{2-}_{ads,ed} \rightleftarrows O^{2-}_{bulk,ed}$
1.8		$O^{2-}_{bulk,ed} \rightleftarrows O^{2-}_{TPB,ed}$	$O^{2-}_{bulk,ed} \rightleftarrows O^{2-}_{TPB,ed}$
		Hydrogen path	
2.1	$H^+_{bulk,et} \rightleftarrows H^+_{g.b.,et}$	$H^+_{bulk,et} \rightleftarrows H^+_{g.b.,et}$	$H^+_{bulk,et} \rightleftarrows H^+_{g.b.,et}$
2.2	$H^+_{g.b.,et} \rightleftarrows H^+_{surf,et}$	$H^+_{g.b.,et} \rightleftarrows H^+_{surf,et}$	$H^+_{g.b.,et} \rightleftarrows H^+_{surf,et}$
2.3	$H^+_{g.b.,et} \rightleftarrows H^+_{TPB,et}$	$H^+_{g.b.,et} \rightleftarrows H^+_{TPB,et}$	$H^+_{g.b.,et} \rightleftarrows H^+_{TPB,et}$
2.4	$H^+_{surf,et} \rightleftarrows H^+_{TPB,et}$	$H^+_{surf,et} \rightleftarrows H^+_{TPB,et}$	$H^+_{surf,et} \rightleftarrows H^+_{TPB,et}$
2.5			$H^+_{surf,et} \rightleftarrows H^+_{int,et}$
2.6			$H^+_{int,et} \rightleftarrows H^+_{int,ed}$
2.7			$H^+_{int,ed} \rightleftarrows H^+_{bulk,ed}$
2.8			$H^+_{bulk,ed} \rightleftarrows H^+_{surf,ed}$
		Electron path	
3.1	$e'_{bulk,ed} \rightleftarrows e'_{TPB,ed}$	$e'_{bulk,ed} \rightleftarrows e'_{TPB,ed}$	$e'_{bulk,ed} \rightleftarrows e'_{TPB,ed}$
3.2	$e'_{bulk,ed} \rightleftarrows e'_{surf,ed}$	$e'_{bulk,ed} \rightleftarrows e'_{surf,ed}$	$e'_{bulk,ed} \rightleftarrows e'_{surf,ed}$
		TPB region	
4	$O_{TPB,\ ed} + 2\,H^+_{TPB,et} + 2\,e'_{TPB,ed} \rightleftarrows H_2O$	$O_{TPB,\ ed} + 2\,H^+_{TPB,et} + 2\,e'_{TPB,ed} \rightleftarrows H_2O$	$O_{TPB,\ ed} + 2\,H^+_{TPB,et} + 2\,e'_{TPB,ed} \rightleftarrows H_2O$
5	$O^{2-}_{TPB,ed} + 2\,H^+_{TPB,et} \rightleftarrows H_2O$	$O^{2-}_{TPB,ed} + 2\,H^+_{TPB,et} \rightleftarrows H_2O$	$O^{2-}_{TPB,ed} + 2\,H^+_{TPB,et} \rightleftarrows H_2O$
		Region of the electrode's surface	
6			$O_{ads,\ ed} + 2\,H^+_{surf,ed} + 2\,e'_{surf,\ ed} \rightleftarrows H_2O$
7			$O^{2-}_{ads,ed} + 2\,H^+_{surf,ed} \rightleftarrows H_2O$

Note. The localisation of the formed water molecules (adsorbed or gas) is not shown. The stages associated with gas diffusion in pores are excluded from consideration. Abbreviations: ads — adsorbed, bulk — grains of polycrystalline materials, g.b. — grain boundary of polycrystalline materials, surf — surface, int — phase interface, et — electrolyte, ed — electrode.

behaviour of these electrodes is theoretically analysed, then the experimental data are presented for the proton-conducting systems of different design (symmetrical cells and fuel cells).

4.1. Electrochemical activity features

As illustrated in Fig. 5, the overall half-reaction occurring at the oxygen electrode can be presented as

$$\frac{1}{2}O_2 + 2e' + 2H^+ \longrightarrow H_2O \qquad (15)$$

Known as ORR, this represents the most common form of the special cases described by Eqs. 10 – 13. Many research efforts have been devoted to improving the electrochemical activity of the electrodes with respect to the ORR. This aim can be advanced using different strategies, details of which will be further clarified when discussing the mechanism of ongoing electrode processes.

The main elementary stages taking place for three different electrode systems being in contact with a proton-conducting electrolyte are summarised in Table 4. As can be seen, a transition from simple-model electrodes with electronic transfer (for example, Pt, LSM) to triple-conducting analogues [for example, M-doped $Ba(Ce,Zr)O_3$] considerably increases the number of electrochemically-active parts. This is the reason why multi-conducting oxides are preferable for applied field. It should be pointed out that electron transfer is not rate-limiting stage due to the higher mobility of electrons compared with protons and oxygen ions. When considering the ionic charge carriers, the mobility of protons is also higher than that of oxygen ions,[188] owing to the lower mass and size of the former. This means that oxygen-involving stages generally regulate the overall electrode performance regardless of nature of the electrodes. In particular, numerous studies [142, 189 – 197] have shown that oxygen diffusion (stages 1.5, 1.7 or 1.8 in Table 4), charge transfer (stages 1.4 or 1.6), oxygen dissociation (stage 1.2) and adsorption of electrochemically active gas components (stage 1.1) can be rate-limiting steps of the resulting reaction(s) (stages 4 – 7).

From the foregoing discussion, the following strategies for preparing electrodes having a desirable electrochemical activity can be proposed:

1. Technological modification (Fig. 10 *a*) aimed at extending the TPB by adding new phase(s) having a different type of conductivity with respect to the basic backbones (matrix) or using nano-sized powders instead of those having sub-micro and micro-sized particles.

2. Functional tuning (Fig. 10 *b*) consisting in the design of materials having a higher activity towards oxygen transport within the bulk of a solid-state particle (oxygen diffusion coefficient, D) and between the particle and the gas media (oxygen surface exchange constant, k).

3. Insertion of additional charge carriers in the electrolyte/electrode system. As shown in Table 4, the highest number of electrode pathways is observed for triple-conducting electrodes.

Since two first strategies are quite adequately discussed in the literature, the next subsections will be devoted to the third one.

4.2. Symmetrical cells

Barium cerates and zirconates heavily doped with M transition elements have been studied as possible electrodes for protonic ceramic electrochemical cells. Initially, it makes sense to reveal their activity in cells with a symmetric configuration, when the same electrode is deposited onto the opposite side of an electrolyte forming a three-layered structure. Then, this structure can be electrochemically characterised by means of electrochemical impedance spectroscopy analysis.

Table 5 lists target values obtained for the Fe- and Co-doped $Ba(Ce,Zr)O_3$ electrodes. Since their polarisation resistances are rather high at low temperatures (below 600 °C), they can be considered as sufficient at higher temperatures (650 and 700 °C), which, however, belong to the intermediate-temperature range. A possible reason of the high R_p for such doped cerates and zirconates might be an insufficient combination of oxygen heteroexchange parameters compared to those of conventional electrode

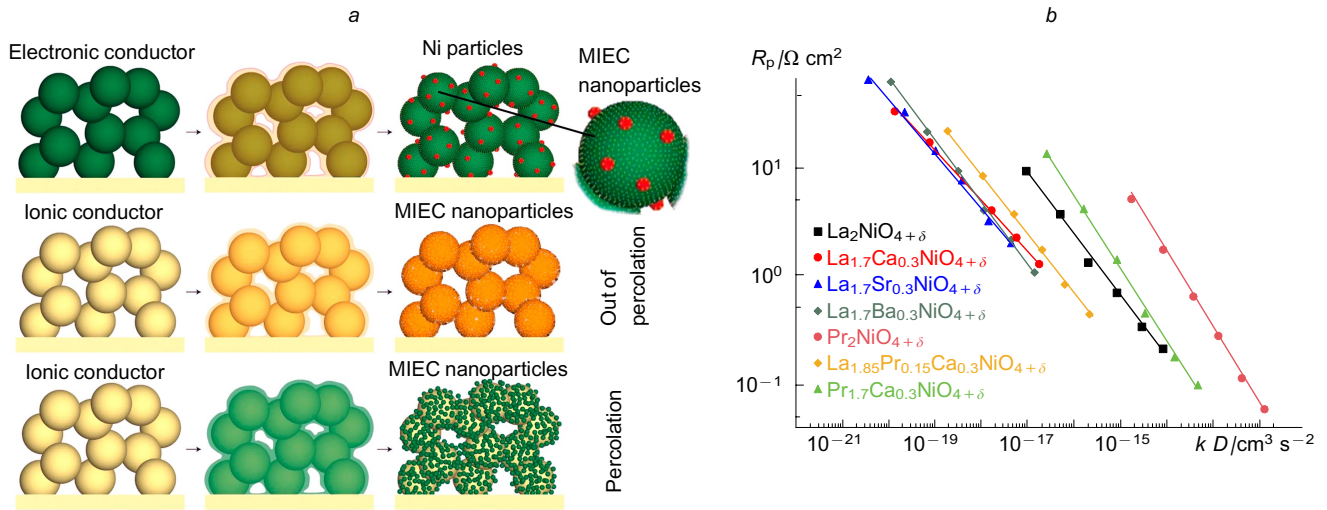


Figure 10. (*a*) Conceptual examples of electrode microstructure development using an infiltration procedure (first step) followed by annealing (second step):[59, 198] the top, central and bottom schemes demonstrate the formation of electrodes with dispersed phases, a mosaic-like structure and continuously connected sediments, respectively. (*b*) Relationship between polarisation resistances of the $Ln_2NiO_{4+\delta}$-based electrodes with oxygen heteroexchange parameters (k and D).[199]

Table 5. Polarisation resistance for the Fe- and Co-doped $Ba(Ce,Zr)O_3$ electrodes of the symmetrical electrode/electrolyte/electrode cells at different temperatures

Electrode	Electrolyte	R_p /Ω cm^2			Ref.
		600 °C	650 °C	700 °C	
$BaCe_{0.4}Sm_{0.2}Fe_{0.4}O_{3-\delta}$	$BaCe_{0.8}Sm_{0.2}O_{3-\delta}$	1.75	0.62	0.23	71
$BaCe_{0.4}Sm_{0.2}Co_{0.4}O_{3-\delta}$	$BaCe_{0.8}Sm_{0.2}O_{3-\delta}$	2.19	0.82	0.37	99
$BaCe_{0.4}Sm_{0.2}Co_{0.4}O_{3-\delta}$ + Ag collector	$BaCe_{0.8}Sm_{0.2}O_{3-\delta}$	1.28	0.54	0.26	99
$BaCo_{0.4}Fe_{0.4}Zr_{0.2}O_{3-\delta}$	$BaZr_{0.1}Ce_{0.7}Y_{0.1}Yb_{0.1}O_{3-\delta}$	0.77	0.37	–	86
$BaCo_{0.4}Fe_{0.4}Zr_{0.2}O_{3-\delta}$	$BaZr_{0.1}Ce_{0.7}Y_{0.1}Yb_{0.1}O_{3-\delta}$	5.30	2.49	1.19	88
$BaCo_{0.4}Fe_{0.4}Zr_{0.15}Y_{0.05}O_{3-\delta}$	$BaZr_{0.1}Ce_{0.7}Y_{0.1}Yb_{0.1}O_{3-\delta}$	2.45	1.10	0.54	88
$BaCo_{0.4}Fe_{0.4}Zr_{0.1}Y_{0.1}O_{3-\delta}$	$BaZr_{0.1}Ce_{0.7}Y_{0.1}Yb_{0.1}O_{3-\delta}$	2.06	0.87	0.46	88
$BaCo_{0.4}Fe_{0.4}Zr_{0.05}Y_{0.15}O_{3-\delta}$	$BaZr_{0.1}Ce_{0.7}Y_{0.1}Yb_{0.1}O_{3-\delta}$	2.83	1.42	0.65	88
$BaCo_{0.4}Fe_{0.4}Zr_{0.1}Y_{0.1}O_{3-\delta}$	$BaZr_{0.1}Ce_{0.7}Y_{0.1}Yb_{0.1}O_{3-\delta}$	1.26	0.69	0.42	121
$BaCo_{0.4}Fe_{0.4}Zr_{0.1}Y_{0.1}O_{3-\delta}$	$BaZr_{0.1}Ce_{0.7}Y_{0.2}O_{3-\delta}$	0.56	0.28	0.09	89
$BaCo_{0.4}Fe_{0.4}Zr_{0.1}Y_{0.1}O_{3-\delta}$	$BaZr_{0.1}Ce_{0.7}Y_{0.1}Yb_{0.1}O_{3-\delta}$	0.31	0.13	–	100
$BaCo_{0.7}(Ce_{0.8}Y_{0.2})_{0.3}O_{3-\delta}$	$BaZr_{0.1}Ce_{0.7}Y_{0.1}Yb_{0.1}O_{3-\delta}$	0.55	0.11	–	100

systems, such as $(Ba,Sr)(Co,Fe)O_3$, doped $LnBaCo_2O_{5+\delta}$, doped $Ln_2NiO_{4+\delta}$.

4.3. Protonic ceramic fuel cells

If, in a symmetrical cell configuration, the M-doped $Ba(Ce,Zr)O_3$ electrodes are located within one gas atmosphere, their operation in fuel cell mode is closer to real conditions. We found more than 20 sets of laboratory data on PCFCs composed of the considered electrode materials. These data are summarised in details in Table 6 and visualised in Fig. 11.

Although a limited sample, the M-doped $Ba(Ce,Zr,Y)O_3$ system demonstrates a tendency towards a decrease in polarisation resistance owing to improved electrochemical activity with respect to ORR (Fig. 11 *a*). As a result, the maximal power density of PCFCs also tends to increase (Fig. 11 *b*). This again agrees well with the percolation theory mentioned in Section 3.4.

Interesting results are associated with a high concentration of cobalt and/or iron ($0.7 \leqslant x \leqslant 0.9$) in $Ba(Ce,Zr,Y)O_3$. Here a R_p deviation of 1 order of magnitude and P_{max} deviations of about 4 times may be observed. Such differences for systems having similar electrolyte and electrode compositions imply that microstructural parameters might play a key role in the electrode kinetic.[202 – 204] However, such parameters are difficult to identify due to a lack of qualitative assessment of the electrodes' microstructure in the provided works. As can be seen from Figs 4, 6 *a* and 10 *a*, the further improvement of the electrode kinetic might be realised by an increase in the TPB length (utilisation of nano-sized particles, infiltration, exsolution methods, formation of the well-adhered electrode layers by tailoring operation regimes such as time and temperature, adjustment of the sparing modes of PCFCs/PCECs related to the reduced chemical-type strain effects for all the functional materials) or its expansion up to the electrode's surface (design of new triple-conducting materials with more pronounced proton transportation).

Considering the most promising results, some attractive electrode materials can be identified. This group includes the BCFZY composition, which has been successfully utilised by Duan *et al.*[167] The fabricated PCFC was able to yield a maximal power density of 660, 620 and 590 mW cm^{-2} at 600 °C with hydrogen, ammonia or methanol, respectively, being used as a fuel (Fig. 12 *a*). Moreover, such a cell showed high tolerance to carbonisation of

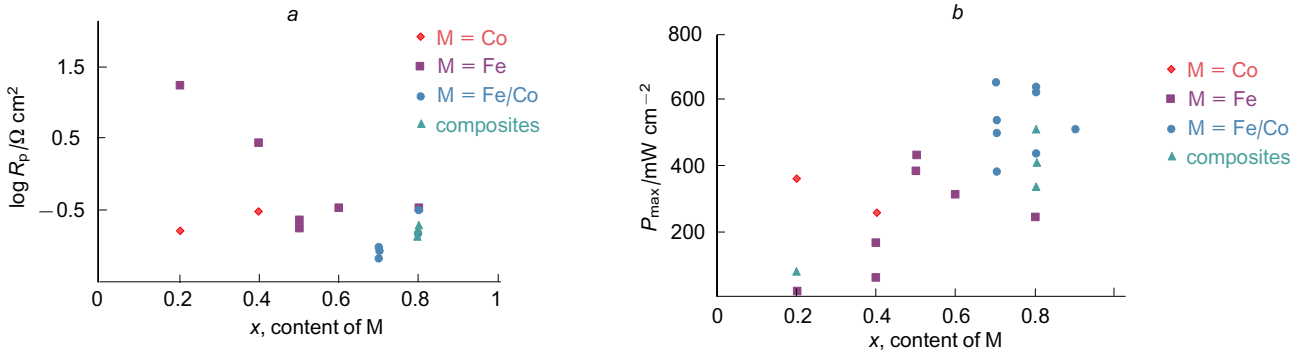


Figure 11. Polarisation resistance (*a*) and maximal power density (*b*) of the fabricated PCFCs at 700 °C depending on the M-concentration in M-doped $Ba(Ce,Zr,Y)O_3$ cathodes. These data are taken from Table 6.[72, 75, 83, 87, 90, 97, 98, 101, 121, 200, 201]

Table 6. Design and electrochemical characteristics of PCFCs with the considered electrode systems: h is the electrolyte thickness, OCV is the open circuit voltage, R_O, R_p and R_{total} are the ohmic, polarisation and total resistances, P_{max} is the maximal power density.

Design of cell (Anode|Electrolyte (h, μm)|Cathode)	Electrochemical characteristics										Ref.
	OCV /V		R_o /Ω cm^2		R_p /Ω cm^2		R_{total} /Ω cm^2		P_{max} /mW cm^{-2}		
	600 °C	700 °C	600 °C	700 °C	600 °C	700 °C	600 °C	700 °C	600 °C	700 °C	
Pt|BCS (300)|BCSF	0.981	0.964	–	–	–	–	–	–	29	62	89
Ni – BCZYYb|BCZYYb (30)|BFCC	1.08	–	1.09	–	0.3	–	1.39	–	257	–	85
Ni – BCZY|BCZY (25)|BCFB	1.034	0.988	0.317	0.22	0.433	0.098	0.75	0.318	362	736	82
Ni – BCZY|BCZY (60)|BZCC	–	1.04	–	0.300	–	0.16	–	0.46	–	370	97
Ni – BCY|BCY(750)|BCCY′ – LCSF	1.182	1.123	–	–	–	–	–	–	44	76	98
Ni – BCZY|BCZY (25)|BCF	1.036	0.986	0.68	0.41	0.8	0.17	1.48	0.58	192	395	75
Ni – BCZY|BCZY (25)|BCF	1.007	0.96	0.461	0.262	1.126	0.224	1.587	0.486	198	443	83
Ni – BCZY|BCZY (25)|BCFB0.1	0.992	0.965	0.358	0.202	0.696	0.078	1.054	0.28	285	707	83
Ni – BCZY|BCZY (25)|BCFB0.2	0.988	0.956	0.265	0.199	0.386	0.061	0.651	0.26	371	943	83
Ni – BCZY|BCZY (25)|BCFB0.3	0.981	0.936	0.307	0.21	0.515	0.099	0.822	0.309	323	617	83
Ni – BCZY|BCZY (25)|BCB	0.989	0.956	0.678	0.44	1.583	0.26	2.261	0.7	127	321	84
Ni – BCS|BCS (70)|BCSF	1.06	1.00	–	–	–	–	–	–	98	169	72
Ni – BCZYYb|BCZYYb (60)|BCFZ	0.97	–	1.57	–	0.68	–	2.25	–	225	–	86
Ni – BCZY|BCZY (25)|BCP	1.026	0.988	0.69	0.48	0.72	0.16	1.41	0.64	179	378	102
Ni – BCZY|BCZY (25)|$B_{0.9}$CFZY	0.98	0.96	0.32	0.21	1.66	0.32	1.98	0.53	166	452	87
Ni – BCZY|BCZY (25)|BCFZY – BCZY	1.01	0.98	0.37	0.23	0.68	0.14	1.05	0.37	244	537	
Ni – BZY|BZY (20)|BCFZY	1.015	–	–	–	–	–	–	–	660	–	167
Ni – BCZYYb|BCZYYb (20)|BCFZY – BCZY63	1.073	–	0.41	–	0.06	–	0.47	–	598	–	88
Ni – BZY|BZY (20)|BCFZY	0.992	–	0.31	–	0.05	–	0.36	–	475	–	88
Ni – BCZYYb|BCZYYb (17)|BCFZY – BCZYYb	1.04	0.985	–	–	0.63	0.17	–	–	150	350	121
Ni – BCZYYb|BCZYYb (17)|BCFZY – BCZYYb + SDC infiltrated	0.961	0.979	–	–	0.99	0.19	–	–	180	430	121
Ni – BCZY|BCZY (40)|BCFZY	1.07	–	0.07	–	0.18	–	0.37	–	482	–	89
Ni – BCZY|BCZY (40)|$B_{0.9}$CFZY	1.063	–	0.09	–	0.49	–	0.56	–	669	–	89
Ni – BZCY35|BZCY35 (14)|$BC_{0.2}$FZ	–	0.943	–	–	0.495	0.149	–	–	–	395	90

Table 6 (continued).

Design of cell (Anode|Electrolyte (*h*, μm)|Cathode)	Electrochemical characteristics										Ref.
	OCV /V		R_o /Ω cm^2		R_p /Ω cm^2		R_{total} /Ω cm^2		P_{max} /mW cm^{-2}		
	600 °C	700 °C	600 °C	700 °C	600 °C	700 °C	600 °C	700 °C	600 °C	700 °C	
Ni – BZCY35|BZCY35 (14)|$BC_{0.3}FZ$	–	0.948	–	–	0.263	0.0917	–	–	–	521	90
Ni – BZCY35|BZCY35 (14)|$BC_{0.4}FZ$	1.015	0.959	0.320	0.245	0.226	0.067	0.546	0.312	444	679	90
Ni – BZCY35|BZCY35 (14)|$BC_{0.5}FZ$	–	0.966	–	–	0.318	0.0819	–	–	–	556	90
Ni – BZCY442|BZCY442|BCCY	1.022	–	0.49	–	0.16	–	0.65	–	399	–	100
Ni – BCZYYb|BCZYYb (16.1)|BCCY	1.075	–	0.20	–	0.13	–	0.33	–	743	–	100
Ni – BCZY53|BCZY53 (20)|BZC64	–	0.95	–	0.58	–	0.29	–	0.86	–	268	101
Ni – BCZY|BCZY (23)|BZF0.2Y	–	0.977	16.8	8.2	60	14.6	76.8	22.8	3	13	200
Ni – BCZY|BCZY (28)|BZF0.4Y	–	0.979	4.6	2.4	12.5	2.4	17.1	4.8	15	53	200
Ni – BCZY|BCZY (21)|BZF0.6Y	–	0.952	0.5	0.3	1.1	0.35	1.6	0.65	170	322	200
Ni – BCZY|BCZY (39)|BZF0.8Y	–	0.963	0.7	0.6	1.9	0.35	2.6	0.95	120	248	200
Ni – BCZYYb|BCZYYb (30)|BCFC	1.02	0.94	0.38	–	0.17	–	0.55	–	440	530	201
Ni – BCZYYb|BCZYYb (30)|BCFCY	1.08	0.99	0.39	–	0.13	–	0.52	–	480	650	201
Ni – BCZYYb|BCZYYb (30)|BCFCG	1.09	1.00	0.38	–	0.12	–	0.50	–	505	660	201

Note. Cathodes: BCSF — $BaCe_{0.4}Sm_{0.2}Fe_{0.4}O_{3-\delta}$, BFCC — $BaFe_{0.6}Co_{0.3}Ce_{0.1}O_{3-\delta}$, BCFB — $BaCe_{0.5}Fe_{0.3}Bi_{0.2}O_{3-\delta}$, BZCC — $BaZr_{0.1}Ce_{0.7}Co_{0.2}O_{3-\delta}$, BCCY′ – LCSF — $BaCe_{0.7}Co_{0.2}Y_{0.1}O_{3-\delta}$ – $La_{0.6}Sr_{0.4}Co_{0.2}Fe_{0.8}O_{3-\delta}$, BCF — $BaCe_{0.5}Fe_{0.5}O_{3-\delta}$, BCFB$x$ (x = 0, 0.1, 0.2 and 0.3) — $BaCe_{0.5}Fe_{0.5-x}Bi_xO_{3-\delta}$, BCB — $BaCe_{0.5}Bi_{0.5}O_{3-\delta}$, BCFZ — $BaCo_{0.4}Fe_{0.4}Zr_{0.2}O_{3-\delta}$, BCFZY — $BaCo_{0.4}Fe_{0.4}Zr_{0.1}Y_{0.1}O_{3-\delta}$, BCP — $BaCe_{0.6}Pr_{0.4}O_{3-\delta}$, BCCY — $BaCo_{0.7}(Ce_{0.8}Y_{0.2})_{0.3}O_{3-\delta}$, $B_{0.9}$CFZY — $Ba_{0.9}Co_{0.4}Fe_{0.4}Zr_{0.1}Y_{0.1}O_{3-\delta}$, BC$x$FZ ($x$ = 0.2, 0.3, 0.4 and 0.5) — $BaCo_xFe_{0.7-x}Zr_{0.3}O_{3-\delta}$, BZC64 — $BaZr_{0.6}Co_{0.4}O_{3-\delta}$, BZF$x$Y ($x$ = 0.2, 0.4, 0.6 and 0.8) — $BaCo_{0.8-x}Fe_xY_{0.2}O_{3-\delta}$, BCFC — $BaCo_{0.4}Fe_{0.5}Ce_{0.1}O_{3-\delta}$, BCFCY — $BaCo_{0.4}Fe_{0.4}Ce_{0.1}Y_{0.1}O_{3-\delta}$, BCFCG — $BaCo_{0.4}Fe_{0.4}Ce_{0.1}Gd_{0.1}O_{3-\delta}$; Electrolytes: BCS — $BaCe_{0.8}Sm_{0.2}O_{3-\delta}$, BCY — $BaCe_{0.8}Y_{0.2}O_{3-\delta}$, BCZYYb — $BaCe_{0.7}Zr_{0.1}Y_{0.1}Yb_{0.1}O_{3-\delta}$, BCZY — $BaCe_{0.7}Zr_{0.1}Y_{0.2}O_{3-\delta}$, BZY — $BaZr_{0.8}Y_{0.2}O_{2-\delta}$, BZCY442 — $BaZr_{0.4}Ce_{0.4}Y_{0.2}O_{3-\delta}$, BZCY63 — $BaCe_{0.6}Zr_{0.3}Y_{0.1}O_{3-\delta}$, BZCY35 — $BaZr_{0.3}Ce_{0.5}Y_{0.2}O_{3-\delta}$, SDC — $Ce_{0.8}Sm_{0.2}O_{2-\delta}$.

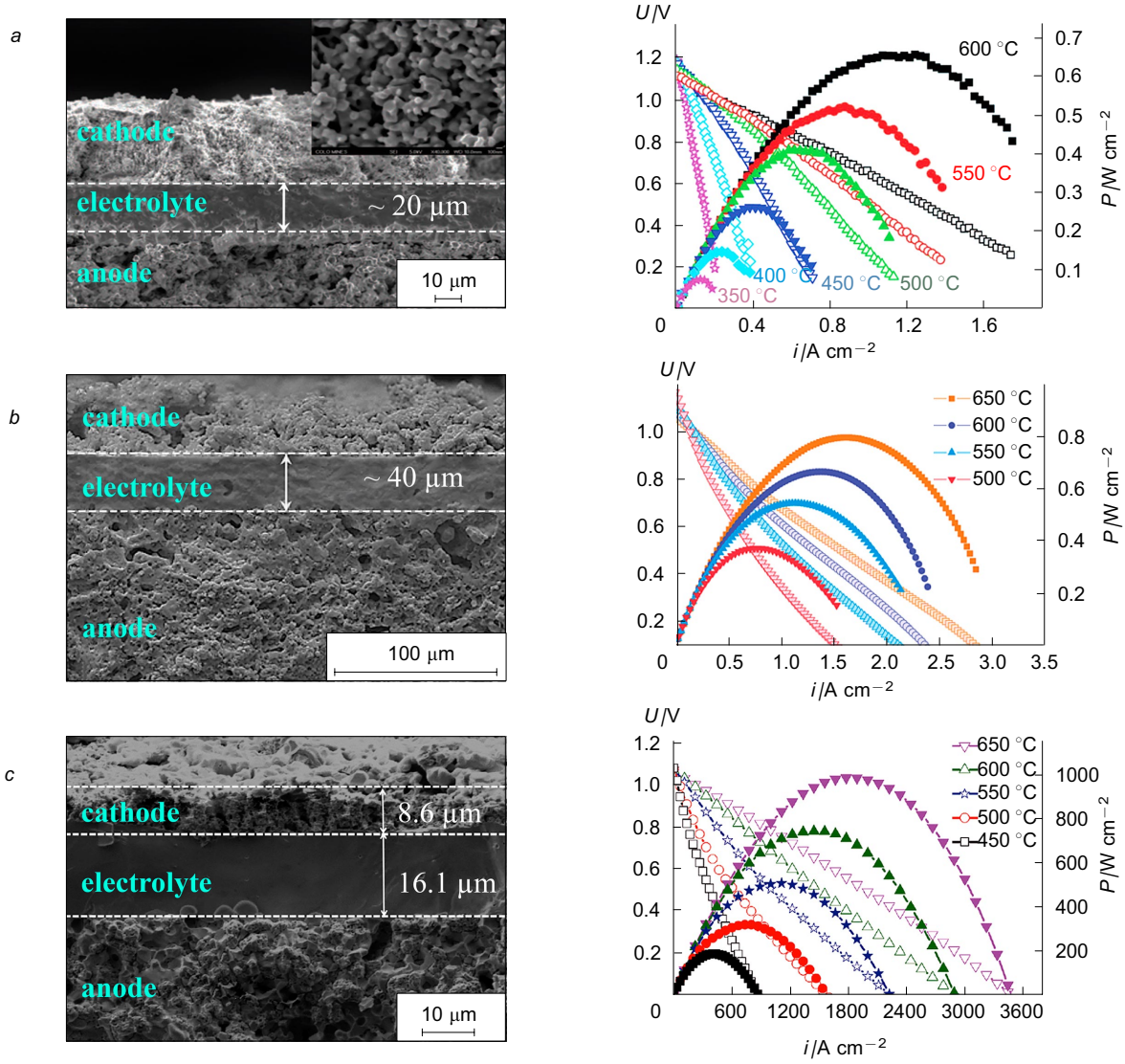


Figure 12. Cross-section microstructures (left) and performances (right) of the best examples of PCFCs selected from Table 6: Ref. 167 (*a*), Ref. 89 (*b*), Ref. 100 (*c*). Here, *i* is the current density, *U* is the voltage, *P* is the power density.

the electrolyte material, inactivity towards sulfur poisoning of Ni particles as a part of Ni-based cermets and excellent thermal stability during ~30 rapid thermal cycles due to the modification of the BCFZY cathode/electrolyte interface. In the work of Ren *et al.*,[89] the electrochemical activity of the BCFZY electrode has been improved by the targeted generation of a Ba-deficiency. Combining the X-ray photoelectron method, thermogravimetric technique and electrical conductivity relaxation, the authors revealed that the Ba-deficiency promoted the oxygen-ion bulk diffusion of BCFZY as a rate-determining step. As a result of better electrode kinetics, power densities of 376, 548, 669 and 797 mW cm^{-2} at 500, 550, 600 and 650 °C, respectively, were achieved (Fig. 12 *b*). Song *et al.*[100] have used a Fe-free composition, $BaCo_{0.7}(Ce_{0.8}\ Y_{0.2})_{0.3}O_{3-\delta}$ (BCCY). In contrast to BCFZY, BCCY is not single-phase, since its one-pot synthesis resulted in the formation of two phases close to $BaCe_{0.8}Y_{0.2}O_{3-\delta}$ and $BaCo_{0.9}(Ce_{0.8}Y_{0.2})_{0.1}O_{3-\delta}$. The former phase conducts protons and electron holes (oxidising conditions), while the latter conducts oxygen ions and holes; this also satisfies the triple-conducting criteria (permitted, however, for multi-phase electrodes). Although the highest performance was reached for the BCCY-based PCFC (Fig. 12 *c*), it is difficult to reproduce certain compositions of $BaCe_{0.8}Y_{0.2}O_{3-\delta}$ and $BaCo_{0.9}(Ce_{0.8}Y_{0.2})_{0.1}O_{3-\delta}$, as well as their weight ratio, using the one-pot synthesis method. Correspondingly, there are difficulties in the reproduction of the real microstructure properties of the BCCY-electrode. In this regard, the design of single-phase triple-conducting materials might seem a more promising approach owing to the reduced number of uncontrolled factors during material preparation and cell testing.

5. Degradation features

In order to achieve commercially competitive conditions for the future commercialisation of protonic ceramic electrochemical cells, it is necessary not only to overcome problems preventing their high performance, but also to address their capability for long-term and thermo-cycling operability. In this regard, cells composed of $Ba(Ce,Zr)O_3$-based functional materials should demonstrate a high stability, at

Table 7. Design and degradation degree of PCFCs with the considered electrode systems: P is potentiometric regime, G is galvanostatic regime, i is the current density, U is the cell potential, T is the temperature, DD is the degradation degree presented in the form of changing the total cell's resistance (ΔR_{total}) for the whole period of time, while degradation rate (DR) is related to 1000 h.

Design of cell (Anode|Electrolyte|Cathode)	Regime	i /U value	τ /h	T /°C	Degradation data				Ref.
					Initial value	Final value	DD (%)	DR (%/1 kh) [a]	
Ni – BCZY|BCZY|BCFB	P	0.7 V	40	600	0.251 W cm^{-2}	0.293 W cm^{-2}	–14.4	–	82
Ni – BCZY|BCZY|BCFB	P	0.7 V	90	650	0.537 W cm^{-2}	0.523 W cm^{-2}	+2.7	–	83
Ni – BCZY|BCZY|BFSB	P	0.7 V	300	600	0.726 A cm^{-2}	0.718 A cm^{-2}	+1.1	3.7	152
Ni – BCZY|BCZY|BCFZY	G	0.06 A cm^{-2}	100	600	0.922 V	0.939 V	+1.8	18.4	87
Ni – BCZYYb|BCZYYb|BCFZY	G	0.3 A cm^{-2}	1100	500	0.812 V	0.847 V	+4.3	3.9	88
Ni – BZY|BZY|BCFZY	G	0.16 A cm^{-2}	500	550	0.763 V	0.731 V	–4.2	–	88
Ni – BCZYYb|BCZYYb|BCFZY – BCZYYb [b]	G	0.45 A cm^{-2}	250	650	1.276 V	1.262 V	–1.1	–	121
Ni – BCZYYb|BCZYYb|BCFZY – BCZYYb	G	0.35 A cm^{-2}	250	650	0.666 V	0.621 V	–6.8	–	121
Ni – BCZY|BCZY|$B_{0.9}$CFZY	G	0.65 A cm^{-2}	120	600	0.585 V	0.566 V	–3.2	–	89
Ni – BCZYYb|BCZYYb|BCCY	G	0.2 A cm^{-2}	800	550	0.815 V	0.819 V	+0.5	0.6	100
Ni – BCZY|BCZY|BZF0.6Y	G	0.15 A cm^{-2}	20	700	0.824 V	0.798 V	–3.1	–	200

Note. Electrolytes: BCZYYb — $BaCe_{0.7}Zr_{0.1}Y_{0.1}Yb_{0.1}O_{3-\delta}$, BCZY — $BaCe_{0.7}Zr_{0.1}Y_{0.2}O_{3-\delta}$, BCS — $BaCe_{0.8}Sm_{0.2}O_{3-\delta}$, BZY — $BaZr_{0.8}Y_{0.2}O_{3-\delta}$; Electrodes: BFCC — $BaFe_{0.6}Co_{0.3}Ce_{0.1}O_{3-\delta}$, BCFB — $BaCe_{0.5}Fe_{0.3}Bi_{0.2}O_{3-\delta}$, BCF — $BaCe_{0.5}Fe_{0.5}O_{3-\delta}$, BCSC — $BaCe_{0.4}Sm_{0.2}Co_{0.4}O_{3-\delta}$, BCFZ — $BaCo_{0.4}Fe_{0.4}Zr_{0.2}O_{3-\delta}$, BSCF — $Ba_{0.5}Sr_{0.5}Co_{0.8}Fe_{0.2}O_{3-\delta}$, BCFZY — $BaCo_{0.4}Fe_{0.4}Zr_{0.1}Y_{0.1}O_{3-\delta}$, BFSB — $BaFe_{0.5}Sn_{0.2}Bi_{0.3}O_{3-\delta}$, $B_{0.9}$CFZY — $Ba_{0.9}Co_{0.4}Fe_{0.4}Zr_{0.1}Y_{0.1}O_{3-\delta}$, BCCY — $BaCo_{0.7}(Ce_{0.8}Y_{0.2})_{0.3}O_{3-\delta}$, BZF0.6Y — $BaZr_{0.2}Fe_{0.6}Y_{0.2}O_{3-\delta}$.

[a] The data are provided for the degraded PCFCs operated not less than 100 h.

[b] The data are provided for electrolysis mode of operation.

least, on account of the excellent chemical compatibility between the electrolyte and the electrodes.

In our attempt to obtain an overview on the experimental results, we have summarised the long-term stability of existing PCFCs (Table 7). These examples show promising results; in particular, the performance of the cells can often be seen to improve rather than degrade over time as evidenced by the variations in the degree of degradation (DD) and degradation rate (DR) parameters. Here, DD is related to the relative change of the output parameters within the studied long-term period, while DR describes the same change but related to 1000 h. Of course, the already mentioned morphological and chemical changes (Fig. 3) occur in all these cases. Nevertheless, it can be seen that these changes can sometimes have a positive effect on the electrochemical performance of the functional materials. For example, Dun *et al.*[88] attributed the observed improvement to the continued reduction of a Ni-based cermet, when the NiO-to-Ni transformation was still not completed during the first 600 h at 500 °C. In some cases,[89, 121] the formal improvement might be associated with the relaxation of the output characteristics during a short period (first hours), while they stabilise in the remaining time range. In that case, the observed changes reflect merely the system equilibration and cannot be attributed to the improvement, since they are not related to morphological/chemical processes.

Among the presented pure results, three unit-type PCFCs showed quite good results (DR less than 5% per 1 kh) on a laboratory scale. However, the DR level can be reduced even up to 1.5% per 1 kh for the large-area PCFCs, as shown by the last results of US[205–207] and Korean laboratories.[208] Here, however, we should point out that such tremendous results come from both materials science and technological achievements, when each stage of the material preparation and cell fabrication is meticulously controlled. Nevertheless, the electrode materials made of $BaCeO_3$-, $BaZrO_3$- or $Ba(Ce,Zr)O_3$-based structural fragments are highly promising owing to the excellent stability of the fabricated electrochemical cells, Fig. 13.

6. Future prospects and concluding remarks

Currently, materials science aspects of the design of protonic ceramic fuel cells and protonic ceramic electrolysis cells are developed to a high degree as means of fabricating low-temperature electrochemical devices demonstrating high levels of efficiency and performance. In order to optimise their operation conditions and long-term life, a rational design of electrode pairs compatible with the proton-conducting electrolytes should be carried out. There are different strategies in the selection of electrode systems, such as Co-free electrodes or Ba-free electrodes; each of these strategies aims at the modification of a certain set of properties. Considering the proton-conducting electrolytes of $BaCeO_3$, $BaZrO_3$ or $BaCeO_3-BaZrO_3$ families [designated as $Ba(Ce,Zr)O_3$], the design of electrodes composed of the same cations at A- and B-positions of the ABO_3 perovskite structure seems to be a possible route for tuning the main functional properties.

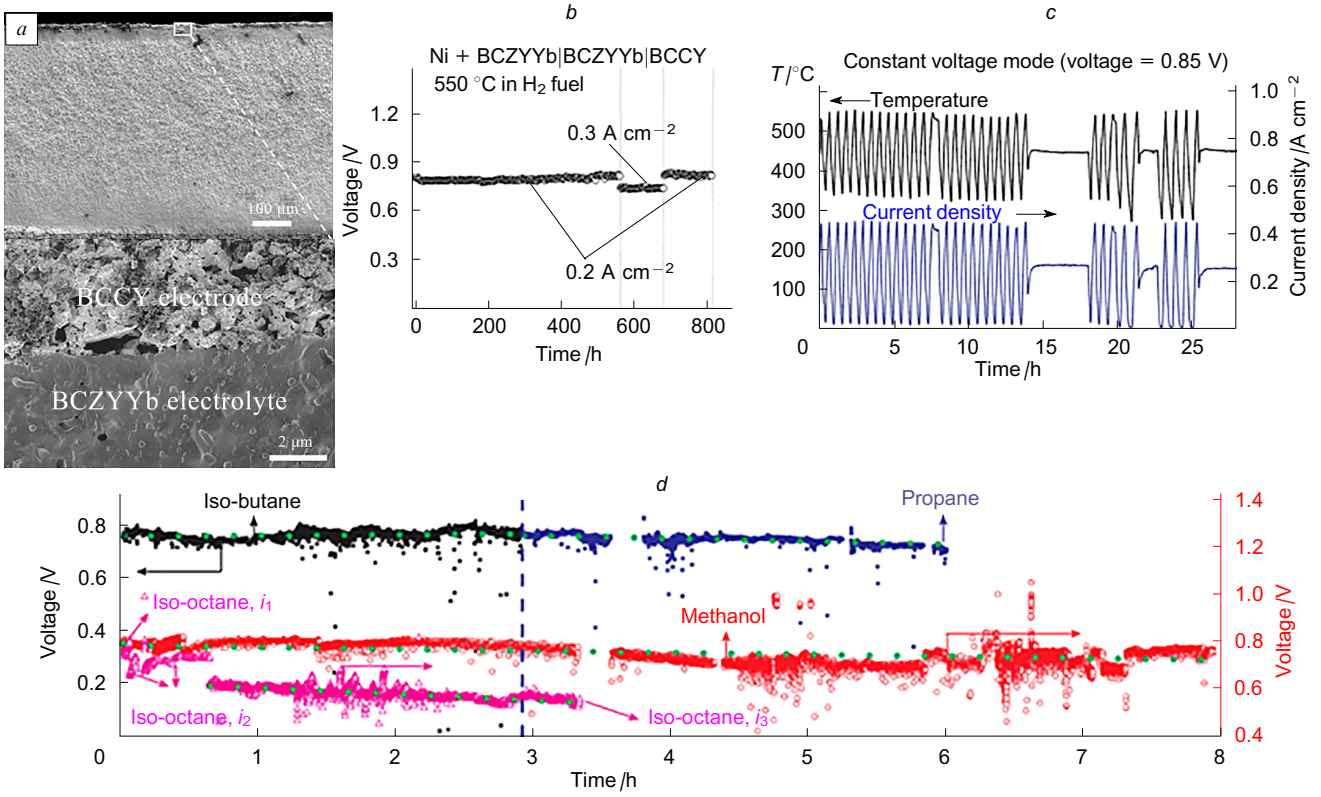


Figure 13. Results of high morphological (*a*), long-term (*b*, *d*) and thermo-cycling (*c*) stabilities of the protonic ceramic electrochemical cells with the M-doped $Ba(Ce,Zr)O_3$-based electrodes. Panel (*d*) represents the long-term stability of the PCFCs operated in atmospheres containing saturated alkanes or methanol. The panels (*a*) and (*b*) were reproduced from Ref. 100, while panels (*c*) and (*d*) were taken from Ref. 167. Here, BCCY = $BaCo_{0.7}(Ce_{0.8}Y_{0.2})_{0.3}O_{3-\delta}$, BCZYYb = $BaCe_{0.7}Zr_{0.1}Y_{0.1}Yb_{0.1}O_{3-\delta}$.

As shown in this review article, a gradual doping of $Ba(Ce,Zr)O_3$ with transition elements (M) has the potential to be used in the development of triple-conducting electrodes having excellent chemical compatibility with the related electrolytes owing to the similarity of their chemical compositions. Moreover, they demonstrate acceptable electrochemical activity in fuel cell operation mode, especially for heavily M-doped representatives. Despite these promising results, such high concentrations might be responsible for the low contribution of proton conductivity and high contribution of the chemical component to the total strain. Nevertheless, some of the PCFCs exhibit outstanding long-term and thermo-cyclic stability of the output performance parameters.

On the basis of the overviewed results, the following lines of research should be further considered in detail:

1. Searching for the optimal concentration of M-dopants in $Ba(Ce,Zr)O_3$, which will be sufficient for achieving the desired functionality of the electrodes.

2. Adopting reliable techniques for the determination of the actual concentration and mobility of the protons in these phases.

3. Studying the microstructural features of the formed electrodes and their influence on overall electrode (and cell) performance.

4. Comprehensive analysis of possible approaches (composites creation, infiltration, exsolution) to improve the electrochemical activity of the electrodes with respect to oxygen reduction reaction.

5. Testing the developed electrodes in electrolysis operation mode.

Fig. 6 *c* and 8 *c* are courtesy of Wiley publishers; Fig. 3 *b*, 6 *b*, 8 *b*, 12 *c*, 13 *a* and 13 *b* are courtesy of Elsevier; Fig. 12 *b* is courtesy of the Royal Society of Chemistry; Fig. 10, 12 *a*, 13 *c* and 13 *d* are courtesy of Springer Nature; Fig. 3 *a* and 8 *d* are courtesy of the Electrochemical Society; Fig. 8 *a* is courtesy of Taylor & Francis Group.

This review work was prepared with the support of the Russian Science Foundation (Grant No. 18-73-00001) and the Council of the President of the Russian Federation (Grant No. MK-1654.2019.3). Dr. Dmitry Medvedev thanks the same funding organisation (Scholarship No. СП 161.2018.1) for supporting his research activity.

References

1. A.B.Yaroslavtsev. *Russ. Chem. Rev.*, **85**, 1255 (2016)
2. Y.Meng, J.Gao, Z.Zhao, J.Amoroso, J.Tong, K.S.Brinkman. *J. Mater. Sci.*, **54**, 9291 (2019)
3. J.Kim, S.Sengodan, S.Kim, O.Kwon, Y.Bu, G.Kim. *Renew. Sus. Energy Rev.*, **109**, 606 (2019)
4. N.L.R.M.Rashid, A.A.Samat, A.A.Jais, M.R.Somalu, A.Muchtar, N.A.Baharuddin, W.N.R.W.Isahak. *Ceram. Int.*, **45**, 6605 (2019)
5. Y.Ling, X.Wang, Z.Ma, K.Wei, Y.Wu, M.Khan, S.Wang. *J. Mater Sci.*, **55**, 1 (2020)
6. N.Kochetova, I.Animitsa, D.Medvedev, A.Demin, P.Tsiakaras. *RSC Adv.*, **6**, 73222 (2016)
7. Y.Okuyama, S.Ikeda, T.Sakai, H.Matsumoto. *Solid State Ionics*, **262**, 865 (2014)
8. A.V.Kasyanova, J.G.Lyagaeva, A.S.Farlenkov, A.I.Vylkov, S.V.Plaksin, D.A.Medvedev, A.K Demin. *J. Eur. Ceram. Soc.*, **40**, 78 (2020)
9. A.V.Kuzmin, A.Yu.Stroeva, V.P.Gorelov, Yu.V.Novikova, A.S.Lesnichyova, A.S.Farlenkov, A.V.Khodimchuk. *Int. J. Hydrogen Energy*, **44**, 1130 (2019)
10. L.A.Dunyushkina, A.A.Pankratov, V.P.Gorelov, A.Brouzgou, P.Tsiakaras. *Electrochim. Acta*, **202**, 39 (2016)
11. R.Shi, J.Liu, H.Wang, F.Wu, H.Miao. *Ceram. Int.*, **43**, 16931 (2017)
12. G.Heras-Juaristi, D.Pérez-Coll, G.C.Mather. *J. Power Sources*, **331**, 435 (2016)
13. N.Tarasova, I.Animitsa. *J. Alloys Compd.*, **739**, 353 (2018)
14. N.Tarasova, Ph.Colomban, I.Animitsa. *J. Phys. Chem. Solids*, **118**, 32 (2018)
15. L.Hakimova, A.Kasyanova, A.Farlenkov, J.Lyagaeva, D.Medvedev, A.Demin, P.Tsiakaras. *Ceram. Int.*, **45**, 209 (2019)
16. Z.Zhu, B.Liu, J.Shen, Y.Lou, Y.Ji. *J. Alloys Compd.*, **659**, 232 (2016)
17. A.V.Shlyakhtina, K.S.Pigalskiy. *Mater. Res. Bull.*, **116**, 72 (2019)
18. A.V.Shlyakhtina, S.N.Savvin, N.V.Lyskov, I.V.Kolbanev, O.K.Karyagina, S.A.Chernyak, L.G. Shcherbakova, P.Núñez. *J. Mater. Chem. A*, **5**, 7618 (2017)
19. I.Sreedhar, B.Agarwal, P.Goyal, S.A.Singh. *J. Electroanal. Chem.*, **848**, 113315 (2019)
20. E.G.Kalinina, E.Y.Pikalova. *Russ. Chem. Rev.*, **88**, 1179 (2019)
21. J.H.Zhu, H.Ghezel-Ayagh. *Int. J. Hydrogen Energy*, **42**, 24278 (2017)
22. M.Irshad, K.Siraj, R.Raza, A.Ali, P.Tiwari, B.Zhu, A.Usman. *Appl. Sci.*, **6**, 75 (2016)
23. R.Pelosato, G.Cordaro, D.Stucchi, C.Cristiani, G.Dotelli. *J. Power Sources*, **298**, 46 (2015)
24. J.H.Kim, A.Manthiram. *J. Mater. Chem. A*, **3**, 24195 (2015)
25. G.Yang, W.Jung, S.J.Ahn, D.Lee. *Appl. Sci.*, **9**, 1030 (2019)
26. Y.H.Lee, I.Chang, G.Y.Cho, J.Park, W.Yu, W.H.Tanveer, S.W.Cha. *Int. J. Pr. Eng. Man-GT*, **5**, 441 (2018)
27. H.Dai, H.Kou, H.Wang, L.Bi. *Electrochem. Commun.*, **96**, 11 (2018)
28. F.J.A.Loureiro, N.Nasani, G.S.Reddy, N.R.Munirathnam, D.P.Fagg. *J. Power Sources*, **438**, 226991 (2019)
29. J.Li, C.Wang, X.Wang, L.Bi. *Electrochem. Commun.*, **112**, 106672 (2020)
30. S.S.Hashim, M.R.Somalu, K.S.Loh, S.Liu, W.Zhou, J.Sunarso. *Int. J. Hydrogen Energy*, **43**, 15281 (2018)
31. L.Lei, J.Zhang, Z.Yuan, J.Liu, M.Ni, F.Chen. *Adv. Funct. Mater.*, **29**, 1903805 (2019)
32. M.A.Pena, J.L.G.Fierro. *Chem. Rev.*, **101**, 1981 (2001)
33. V.M.Goldschmidt. *Naturwissenschaften*, **14**, 477 (1926)
34. Z.Li, M.Yang, J.S.Park, S.H.Wei, J.J.Berry, K.Zhu. *Chem. Mater.*, **28**, 284 (2015)
35. R.D.Shannon. *Acta Crystallogr., Sect. A*, **32**, 751 (1976)
36. H.D.Megaw. *Proc. Phys. Soc.*, **58**, 133 (1946)
37. C.S.Tu, R.R.Chien, V.H.Schmidt, S.C.Lee, C.C.Huang. *J. Phys.: Condens. Matter*, **24** 155403 (2012)
38. G.Heras-Juaristi, U.Amador, R.O.Fuentes, A.L.Chinelatto, J.R.de Paz, C.Ritter, D.P. Fagg, D.Pérez-Coll, G.C.Mather. *J. Mater. Chem. A*, **5**, 5324 (2018)
39. D.Medvedev, J.Lyagaeva, S.Plaksin, A.Demin, P.Tsiakaras. *J. Power Sources*, **273**, 716 (2015)
40. K.Singh, A.K.Baral, V.Thangadurai. *J. Mater. Sci. Res.*, **5**, 34 (2016)
41. T.Norby. *Solid State Ionics*, **40**, 857 (1990)
42. P.Colomban. *Fuel Cells*, **13**, 6 (2013)
43. N.Bonanos. *Solid State Ionics*, **145**, 265 (2001)
44. S.J.Song, E.D.Wachsman, S.E.Dorris, U.Balachandran. *Solid State Ionics*, **149**, 1 (2002)
45. N.Bonanos, F.W.Poulsen. *J. Mater. Chem.*, **9**, 431 (1999)
46. F.J.Loureiro, D.Pérez-Coll, V.C.Graça, S.M.Mikhalev, A.F.Ribeiro, A.Mendes, D.P.Fagg. *J. Mater. Chem. A*, **7**, 18135 (2019)
47. D.A.Medvedev, J.G.Lyagaeva, E.V.Gorbova, A.K.Demin, P.Tsiakaras. *Prog. Mater. Sci.*, **75**, 38 (2016)
48. D.Medvedev. *Int. J. Hydrogen Energy*, **44**, 26711 (2019)

49. V.L.Kozhevnikov, I.A.Leonidov, M.V.Patrakeev. *Russ. Chem. Rev*., **82**, 772 (2013)
50. A.A.Plazaola, A.C.Labella, Y.Liu, N.B.Porras, D.A.P.Tanaka, M.V.S.Annaland, F.Gallucci. *Processes*, **7**, 128 (2019)
51. C.Li, J.J.Chew, A.Mahmoud, S.Liu, J.Sunarso. *J. Membr. Sci*., **567**, 228 (2018)
52. D.Y.Kim, S.Miyoshi, T.Tsuchiya, S. Yamaguchi. *ECS Trans*., **45**, 161 (2012)
53. A.Løken, S.Ricote, S.Wachowski. *Crystals*, **8**, 365 (2018)
54. D.Kim, S.Miyoshi, T.Tsuchiya, S.Yamaguchi. *Solid State Ionics*, **262**, 875 (2014)
55. M.Talimi, V.Thangadurai. *Ionics*, **17**, 195 (2011)
56. T.Shimura, H.Tanaka, H.Matsumoto, T.Yogo. *Solid State Ionics*, **176**, 2945 (2005)
57. M.Reisert, A.Aphale, P.Singh. *Materials*, **11**, 2169 (2018)
58. B.Koo, K.Kim, J.K.Kim, H.Kwon, J.W.Han, W.Jung. *Joule*, **2**, 1476 (2018)
59. P.A.Connor, X.Yue, C.D.Savaniu, R.Price, G.Triantafyllou, M.Cassidy, R.I.Tomov, B.A.Glowacki, R.V.Kumar, J.T.S.Irvine. *Adv. Energy Mater*., **8**, 1800120 (2018)
60. Z.Yang, M.Guo, N.Wang, C.Ma, J.Wang, M.Han. *Int. J. Hydrogen Energy*, **42**, 24948 (2017)
61. H.Yokokawa, M.Suzuki, M.Yoda, T.Suto, K.Tomida, K.Hiwatashi, T.Ryu. *Fuel Cells*, **19**, 311 (2019)
62. S.Ya.Istomin, E.V.Antipov. *Russ. Chem. Rev*., **82**, 686 (2013)
63. K.Eguchi. *J. Jpn. Petrol. Inst*., **58**, 79 (2015)
64. D.K.Niakolas. *Appl. Catal., A: Gen*., **486**, 123 (2014)
65. W.Yue, Y.Li, Y.Zheng, T.Wu, C.Zhao, J.Zhao, G.Geng, W.Zhang, J.Chen, J.Zhu, B.Yu. *Nano Energy*, **62**, 64 (2019)
66. K.Chen, S.P.Jiang. *J. Electrochem. Soc*.,**163**, F3070 (2016)
67. V.Venkataraman, M.Pérez-Fortes, L.Wang, Y.S.Hajimolana, C.Boigues-Muñoz, A.Agostini, S.J.McPhail, F.Maréchal, J.Van Herle, P.V.Aravind. *J. Energy Storage*, **24**, 100782 (2019)
68. J.Kim, S.Sengodan, G.Kwon, D.Ding, J.Shin, M.Liu, G.Kim. *ChemSusChem*, **7**, 2811 (2014)
69. L.Fan, P.C.Su. *J. Power Sources*, **306**, 369 (2016)
70. A.Zhu, G.Zhang, T.Wan, T.Shi, H.Wang, M.Wu, Z.Shao. *Electrochim. Acta*, **259**, 559 (2018)
71. C.Zhang, Z.Du, H. Zhao, X.Zhang. *Electrochim. Acta*, **108**, 369 (2013)
72. C.Zhang, H.Zhao. *J. Mater. Chem*., **22**, 18387 (2012)
73. H.Zhang, A.Suresh, C.B.Carter, B.A.Wilhite. *Solid State Ionics*, **266**, 58 (2014)
74. L.Zhu, T.Hong, C.Xu, J.Cheng. *Int. J. Hydrogen Energy*, **44**, 15400 (2019)
75. Z.Tao, L.Bi, Z.Zhu, W.Liu. *J. Power Sources*, **194**, 801 (2009)
76. S.Escolástico, M.Ivanova, C.Solís, S.Roitsch, W.A.Meulenberg, J.M.Serra. *RSC Adv*., **2**, 4932 (2012)
77. B.Mirfakhraei, F.Ramezanipour, S.Paulson, V.Birss, V.Thangadurai. *Front. Energy Res*., **2**, 9 (2014)
78. P.P.Khirade, S.D.Birajdar, A.V.Humbe, K.M.Jadhav. *J. Electron. Mater*., **45**, 3227 (2016)
79. D.Y.Kim, S.Miyoshi, T.Tsuchiya, S.Yamaguchi. *Chem. Mater*., **26**, 927 (2013)
80. A.V.Kasyanova, A.O.Rudenko, N.G.Molchanova, A.I.Vylkov, J.G.Lyagaeva, D.A.Medvedev. *Mendeleev Commun*., **29**, 710 (2019)
81. W.He, J.Fan, H.Zhang, M.Chen, Z.Sun, M.Ni. *Int. J. Hydrogen Energy,* **44***,* 32164 (2019)
82. D.Shan, Z.Gong, Y.Wu, L.Miao, K.Dong, W.Liu. *Ceram. Int*., **43**, 3660 (2017)
83. Y.Wu, J.Hou, Z.Gong, L.Miao, H.Tang, W.Liu. *J. Alloys Compd*., **790**, 551 (2019)
84. Z.Tao, L.Bi, L.Yan, W.Sun, Z.Zhu, R.Peng, W.Liu. *Electrochem. Commun*., **11**, 688 (2009)
85. L.Zhang, C.Li. *Ceram. Int*., **42**, 10511 (2016)
86. M.Shang, J.Tong, R.O'Hayre. *RSC Adv*., **3**, 15769 (2013)
87. K.Wei, N.Li, Y.Wu, W.Song, X.Wang, L.Guo, Y.Ling. *Ceram. Int*. **45**, 18583 (2019)
88. C.Duan, J.Tong, M.Shang, S.Nikodemski, M.Sanders, S.Ricote, R.O Hayre. *Science*, **349**, 1321 (2015)
89. R.Ren, Z.Wang, C.Xu, W.Sun, J.Qiao, D.W.Rooney, K.Sun. *J. Mater. Chem. A*, **7**, 18365 (2019)
90. H.Lv, Z.Jin, R.Peng, W.Liu, Z.Gong. *Ceram. Int*., **45**, 23948 (2019)
91. L.Zhang, J.Li, J.Yang, H.Shen. *Electrochim. Acta*, **154**, 244 (2015)
92. R.Zohourian, R.Merkle, J.Maier. *Solid State Ionics*, **299**, 64 (2017)
93. X.Kuai, G.Yang, Y.Chen, H.Sun, J.Dai, Y.Song, Z.Shao. *Adv. Energy Mater*., 1902384 (2019)
94. M.Saqib, J.I.Lee, J.Y.Park. *ECS Trans*., **91**, 1503 (2019)
95. W.Yao, H.Cheng, H.Zhao, X.Lu, X.Zou, S.Li, C.Li. *J. Membr. Sci*., **504**, 251 (2016)
96. H.Cheng, W.Yao, X.Lu, Z.Zhou, C.Li, J.Liu. *Fuel Proc. Technol*., **131**, 36 (2015)
97. L.Yang, S.Wang, X.Lou, M.Liu. *Int. J. Hydrogen Energy*, **36**, 2266 (2011)
98. K.Miyazaki, Y.Ding, H.Muroyama, T.Matsui, K.Eguchi, *Electrochemistry*, 19-00039 (2020)
99. C.Zhang, H.Zhao. *Electrochem. Commun*., **13**, 1070 (2011)
100. Y.Song, Y.Chen, W.Wang, C.Zhou, Y.Zhong, G.Yang, Z.Shao. *Joule*, **3**, 2842 (2019)
101. Y.Rao, S.Zhong, F.He, Z.Wang, R.Peng, Y.Lu. *Int. J. Hydrogen Energy*, **37**, 12522 (2012)
102. Z.Tao, G.Hou, N.Xu, X.Chen, Q.Zhang. *Fuel Cells*, **14**, 135 (2014)
103. G.Heras-Juaristi, U.Amador, J.Romero de Paz, R.O.Fuentes, A.L.Chinelatto, C.Ritter, G.C.Mather. *Inorg. Chem*., **57**, 15023 (2018)
104. N.Maffei, L.Pelletier, J.P.Charland, A.McFarlan. *Fuel Cells*, **7**, 323 (2007)
105. R.Mukundan, P.K.Davies, W.L.Worrell. *J. Electrochem. Soc*., **148**, A82 (2001)
106. M.Y.Wang, L.G.Qiu. *Chin. J. Chem. Phys*., **21**, 286 (2008)
107. E.Fabbri, I.Markus, L.Bi, D.Pergolesi, E.Traversa. *Solid State Ionics*, **202**, 30 (2011)
108. E.Fabbri, L.Bi, H.Tanaka, D.Pergolesi, E.Traversa. *Adv. Funct. Mater*., **21**, 158 (2011)
109. M.Morales, V.Miguel-Pérez, A.Tarancón, A.Slodczyk, M.Torrell, B. Ballesteros, A.Morata. *J. Power Sources*, **344**, 141 (2017)
110. V.Miguel-Pérez, A.Martínez-Amesti, M.I.Arriortua. *J. Power Sources*, **280,** 505 (2015)
111. D.Montinaro, A.R.Contino, A.Dellai, M.Rolland. *Int. J. Hydrogen Energy*, **39**, 21638 (2014)
112. D.The, S.Grieshammer, M.Schroeder, M.Martin, M.Al Daroukh, F. Tietz, A.Brisse. *J. Power Sources*, **275**, 901 (2015)
113. B.Singh, S.Ghosh, S.Aich, B. Roy. *J. Power Sources*, **339**, 103 (2017)
114. L.Fan, B.Zhu, P.C.Su, C.He. *Nano Energy*, **45**, 148 (2018)
115. B.S.Prakash, R.Pavitra, S.S.Kumar, S.T.Aruna. *J. Power Sources*, **381**, 136 (2018)
116. I.Jang, S.Kim, C.Kim, H.Lee, H.Yoon, T.Song, U.Paik. *J. Power Sources*, **435**, 226776 (2019)
117. S.Lee, S.Lee, H.J.Kim, S.M.Choi, H.An, M.Y.Park, H.I.Ji. *J. Mater. Chem. A*, **6**, 15083 (2018)
118. A.Mai, M.Becker, W.Assenmacher, F.Tietz, D.Hathiramani, E.Ivers-Tiffée, W.Mader. *Solid State Ionics*, **177**, 1965 (2006)
119. V.Wilde, H.Störmer, J.Szász, F.Wankmüller, E.Ivers-Tiffée, D.Gerthsen. *ACS Appl. Energy Mater*., **1**, 6790 (2018)
120. J.T.Chou, Y.Inoue, T.Kawabata, J.Matsuda, S.Taniguchi, K.Sasaki. *J. Electrochem. Soc*., **165**, F959 (2018)
121. M.Saqib, J.I.Lee, J.S.Shin, K.Park, Y.D.Kim, K.B.Kim, J.Y.Park. *J. Electrochem. Soc*., **166**, F746 (2019)

122. S.R.Bishop, H.L.Tuller, Y.Kuru, B.Yildiz. *J. Eur. Ceram. Soc.,* **31**, 2351 (2011)
123. W.Wang, D.Medvedev, Z.Shao. *Adv. Funct. Mater.*, **28**, 1802592 (2018)
124. E.V.Tsipis, V.V.Kharton. *J. Solid State Electrochem.*, **12**, 1367 (2008)
125. A.V.Kuzmin, Y.V.Novikova, A.Y.Stroeva, V.P.Gorelov, A.I.Vylkov, M.V.Ananiev, Y.P.Zaikov. *Russ. J. Appl. Chem.*, **91**, 196 (2018)
126. T.Nakamura, K.Yashiro, K.Sato, J.Mizusaki. *Solid State Ionics*, **181**, 292 (2010)
127. E.Niwa, T.Hashimoto. *Solid State Ionics*, **285**, 187 (2016)
128. J.Sheth, D.Chen, J.J.Kim, W.J.Bowman, P.A.Crozier, H.L.Tuller, S.R.Bishop. *Nanoscale*, **8**, 16499 (2016)
129. N.H.Perry, J.J.Kim, S.R.Bishop, H.L.Tuller. *J. Mater. Chem. A*, **3**, 3602 (2015)
130. X.Huang, J.Feng, H.R.Abdellatif, J.Zou, G.Zhang, C.Ni. *Int. J. Hydrogen Energy*, **43**, 8962 (2018)
131. V.Tsidilkovski, A.Kuzmin, L.Putilov, V. Balakireva. *Solid State Ionics*, **301**, 170 (2017)
132. D.Han, N.Hatada, T.Uda. *J. Am. Ceram. Soc.*, **99**, 3745 (2016)
133. A.K.Andersson, S.M.Selbach, C.S.Knee, T.Grande. *J. Am. Ceram. Soc.*, **97**, 2654 (2014)
134. S.R.Bishop, D.Marrocchelli, C.Chatzichristodoulou, N.H.Perry, M.B. Mogensen, H.L.Tuller, E.D.Wachsman. *Annu. Rev. Mater. Res.*, **44**, 205 (2014)
135. A.Herklotz, D.Lee, E.J.Guo, T.L.Meyer, J.R.Petrie, H.N.Lee. *J. Phys. Condens. Matter.*, **29**, 493001 (2017)
136. E.Jedvik, A.Lindman, M.R.Benediktsson, G.Wahnström. *Solid State Ionics*, **275**, 2 (2015)
137. A.Dubois, K.Taghikhani, J.R.Berger, H.Zhu, R.P.O'Hayre, R.J.Braun, S.Ricote. *J. Electrochem. Soc.*, **166**, F1007 (2019)
138. J.Lyagaeva, D.Medvedev, A.Demin, P.Tsiakaras. *J. Power Sources*, **278**, 436 (2015)
139. C.Duan, D.Hook, Y.Chen, J.Tong, R.O'Hayre. *Energy Environ. Sci.*, **10**, 176 (2017)
140. G.Yang, J.Shen, Y.Chen, M.O.Tadé, Z. Shao. *J. Power Sources*, **298**, 184 (2015)
141. C.G.Moura, J.P.D.F.Grilo, D.A.Macedo, M.R.Cesário, D.P.Fagg, R.M.Nascimento. *Mater. Chem. Phys.*, **180**, 256 (2016)
142. A.Tarutin, J.Lyagaeva, A.Farlenkov, S.Plaksin, G.Vdovin, A.Demin, D.Medvedev. *Materials*, **12**, 118 (2019)
143. L.Li, F.Jin, Y.Shen, T.He. *Electrochim. Acta*, **182**, 682 (2015)
144. B.He, C.Gong, Z.Wang, L.Jia, L.Zhao. *Int. J. Hydrogen Energy*, **42**, 10308 (2017)
145. N.Danilov, E.Pikalova, J.Lyagaeva, B.Antonov, D.Medvedev, A.Demin, P.Tsiakaras. *J. Power Sources*, **366**, 161 (2017)
146. J.Lyagaeva, N.Danilov, A.Tarutin, G.Vdovin, D.Medvedev, A.Demin, P.Tsiakaras. *Dalton Trans.*, **47**, 8149 (2018)
147. A.S.Urusova, A.V.Bryuzgina, M.Yu.Mychinko, N.E.Mordvinova, O.I.Lebedev, V.Caignaert, E.A.Kiselev, T.V.Aksenova, V.A.Cherepanov. *J. Alloys Compd.*, **694**, 375 (2017)
148. A.S.Urusova, V.A.Cherepanov, T.V.Aksenova, L.Ya.Gavrilova, E.A.Kiselev. *J. Solid State Chem.*, **202**, 207 (2013)
149. T.-H.Park. *J. Korean. Soc. Prec. Eng.,* **35**, 1.1414 (2018)
150. G.Li, Y.Zhang, Y.Ling, B.He, J.Xu, L.Zhao. *Int. J. Hydrogen Energy*, **41**, 5074 (2016)
151. L.R.Tarutina, G.K.Vdovin, J.G.Lyagaeva, D.A.Medvedev. *J. Alloys Compd.*, **831**, 154895 (2020)
152. Y.Xia, Z.Jin, H.Wang, Z.Gong, H.Lv, R.Peng, L.Bi. *J. Mater. Chem. A*, **7**, 16136 (2019)
153. C.Zhou, J.SunarsoY.Song, J.Dai, J Zhang, B.Gu, Z.Shao. *J. Mater. Chem. A*, **7**, 13265 (2019)
154. H.T.Lozano, J.Druce, S.J.Cooper, J.A.Kilner. *Sci. Technol. Adv. Mater.*, **18**, 977 (2017)
155. C.Zhou, J.Sunarso, J.Dai, R.Ran, Y.Song, F.He, W.Zhou, Z.Shao, *J. Membr. Sci.*, **596**, 117709 (2020)
156. N.Tarasova, I.Animitsa. *Solid State Sci.*, **87**, 87 (2019)
157. N.Tarasova, I. Animitsa. *Solid State Ionics*, **317**, 21 (2018)
158. J.Lyagaeva, N.Danilov, D.Korona, A.Farlenkov, D.Medvedev, A.Demin, P.Tsiakaras. *Ceram. Int.*, **43**, 7184 (2017)
159. D.A.Medvedev, E.V.Gorbova, A.K.Demin, P.Tsiakaras. *Int. J. Hydrogen Energy*, **39**, 21547 (2014)
160. M.Bahout, S.S.Pramana, J.M.Hanlon, V.Dorcet, R.I.Smith, S.Paofai, S.J.Skinner. *J. Mater. Chem. A*, **3**, 15420 (2015)
161. F.Brieuc, G.Dezanneau, M.Hayoun, H.Dammak. *Solid State Ionics*, **309**, 187 (2017)
162. A.Seong, J.Kim, J.Kim, S.Kim, S.Sengodan, J.Shin, G.Kim. *J. Electrochem. Soc.*, **165**, F1098 (2018)
163. A.B.Mucoz-García, M.Tuccillo, M.Pavone. *J. Mater. Chem. A*, **5**, 11825 (2017)
164. A.Benes, A.Molinari, R.Witte, R.Kruk, J.Brötz, R.Chellali, O.Clemens. *Materials*, **11**, 52.(2018)
165. D.Poetzsch, R.Merkle, J.Maier. *Phys. Chem. Chem. Phys.*, **16**, 16446 (2014)
166. Y.Chen, T.Hong, P.Wang, K.Brinkman, J.Tong, J.Cheng. *J. Power Sources*, **440**, 227122 (2019)
167. C.Duan, R.J.Kee, H.Zhu, C.Karakaya, Y.Chen, S.Ricote, A.Jarry, E.J.Crumlin, D.Hook, R.Braun, N.P.Sullivan, R.O Hayre. *Nature (London)*, **557**, 217 (2018)
168. R.Zohourian, R.Merkle, G.Raimondi, J.Maier. *Adv. Funct. Mater.*, **28**, 1801241 (2018)
169. C.Xia, Y.Mi, B.Wang, B.Lin, G.Chen, B.Zhu. *Nat. Commun.*, **10**, 1707 (2019)
170. S.Ryu, S.Lee, W.Jeong, A.Pandiyan, S.B.K.Moorthy, I.Chang, S.W.Cha. *Surface Coat. Technol.*, **369**, 265 (2019)
171. R.Strandbakke, V.A.Cherepanov, A.Y.Zuev, D.S.Tsvetkov, C.Argirusis, G.Sourkouni, T.Norby. *Solid State Ionics*, **278**, 120 (2015)
172. F.He, T.Wu, R. Peng, C.Xia. *J. Power Sources*, **194**, 263 (2009)
173. F.He, D.Song, R.Peng, G.Meng, S.Yang. *J. Power Sources*, **195**, 3359 (2010)
174. A.Grimaud, F.Mauvy, J.M.Bassat, S.Fourcade, M.Marrony, J.C.Grenier. *J. Mater. Chem.*, **22**, 16017 (2012)
175. N.Danilov, J.Lyagaeva, G.Vdovin, D.Medvedev. *Appl. Energy*, **237**, 924 (2019)
176. E.Pikalova, A.Kolchugin, M.Koroleva, G.Vdovin, A.Farlenkov, D.Medvedev. *J. Power Sources*, **438**, 226996 (2019)
177. J.Dailly, F.Mauvy, M.Marrony, M.Pouchard, J.C.Grenier. *J. Solid State Electrochem.*, **15**, 245 (2011)
178. A.Grimaud, F.Mauvy, J.M.Bassat, S.Fourcade, L.Rocheron, M.Marrony, J.C.Grenier. *J. Electrochem. Soc.*, **159**, B683 (2012)
179. A.Grimaud, J.M.Bassat, F.Mauvy, M.Pollet, A.Wattiaux, M.Marrony, J.C.Grenier. *J. Mater. Chem. A*, **2**, 3594 (2014)
180. N.Mahato, A.Banerjee, A.Gupta, S.Omar, K.Balani. *Prog. Mater. Sci.*, **72**, 141 (2015)
181. D.A.G.Bruggeman. *Ann. Phys.*, **24** 636 (1935)
182. D.S.McLachlan. *J. Phys. C: Solid State Phys.*, **19**, 1339 (1986)
183. D.S.McLachlan. *J. Electroceram.*, **5**, 93 (2000)
184. N.V.Sharova, V.P. Gorelov. *Russ. J. Electrochem.*, **39**, 461 (2003)
185. N.V.Sharova, V.P.Gorelov, V.B.Balakireva. *Russ. J. Electrochem.*, **41**, 665 (2005)
186. J.Hombo, Y.Matsumoto, T.Kawano. *J. Solid State Chem.*, **84**, 138 (1990)
187. C.Duan, R.Kee, H.Zhu, N.Sullivan, L.Zhu, L.Bian, R.O'Hayre. *Nat. Energy*, **4**, 230 (2019)
188. I.H.Kim, D.K.Lim, H.Bae, A.Bhardwaj, J.Y.Park, S.J.Song. *J. Mater. Chem. A.* **7**, 21321 (2019)
189. A.Tarutin, A.Kasyanova, J.Lyagaeva, G.Vdovin, D.Medvedev. *J. Energ. Chem.*, **40**, 65 (2020)

190. J.Chen, J.Li, L.Jia, I.Moussa, B.Chi, J.Pu, J.Li. *J. Power Sources*, **428**, 13 (2019)
191. D.Clematis, S.Presto, M.P.Carpanese, A.Barbucci, F.Deganello, L.F.Liotta, M.Viviani. *Catalysts*, **9**, 441 (2019)
192. X.Wang, Z.Ma, T.Zhang, J.Kang, X.Ou, P.Feng, Y.Ling. *ACS Appl. Mater. Interfaces*, **10**, 35047 (2018)
193. D.K.Lim, J.H.Kim, A.U.Chavan, T.R.Lee, Y.S.Yoo, S.J.Song. *Ceram. Int.*, **42**, 3776 (2016)
194. S.M.Choi, H.An, K.J.Yoon, B.K.Kim, H.W.Lee, J.W.Son, J.H.Lee. *Appl. Energy*, **233**, 29 (2019)
195. Y.Xie, N.Shi, D.Huan, W.Tan, J.Zhu, X.Zheng, C.Xia. *ChemSusChem*, **11**, 3423 (2018)
196. W.Cai, Y.Guo, T.Zhang, T.Guo, H.Chen, B.Lin, Y.Ling. *Ceram. Int.*, **44**, 14297 (2018)
197. N.Shi, F.Su, D.Huan, Y.Xie, J.Lin, W.Tan, Y.Lu. *J. Mater. Chem. A*, **5**, 19664 (2017)
198. J.T.Irvine, D.Neagu, M.C.Verbraeken, C.Chatzichristodoulou, C.Graves, M.B.Mogensen. *Nat. Energy*, **1**, 15014 (2016)
199. V.A.Sadykov, E.M.Sadovskaya, E.Y.Pikalova, A.A.Kolchugin, E.A.Filonova, S.M.Pikalov, J.M.Bassat. *Ionics*, **24**, 1181 (2018)
200. Y.Wu, K.Li, Y.Yang, W.Song, Z.Ma, H.Chen, Y.Ling. *J. Alloys Compd.*, **814**, 152220 (2019)
201. L.Zhang, S.Yang, S.Zhang, Y.Yang. *Int. J. Hydrogen Energy*, **44**, 27921 (2019)
202. M.Shishkin, T.Ziegler. *Phys. Chem. Chem. Phys.*, **16**, 1798 (2014)
203. A.Bertei, E.Ruiz-Trejo, K.Kareh, V.Yufit, X.Wang, F.Tariq, N.P.Brandon. *Nano Energy*, **38**, 526 (2017)
204. X.Lu, T.M.M.Heenan, J.J.Bailey, T.Li, K.Li, D.J.L.Brett, P.R.Shearing. *J. Power Sources*, **365**, 210 (2017)
205. R.J.Braun, A.Dubois, K.Ferguson, C.Duan, C.Karakaya, R.J.Kee, A.Wood. *ECS Trans.*, **91**, 997 (2019)
206. H.Ding, W.Wu, D.Ding. *ECS Trans.*, **91**, 1029 (2019)
207. S.Choi, C.J.Kucharczyk, Y.Liang, X.Zhang, I.Takeuchi, I.H.Ji, S.M.Haile. *Nat. Energy*, **3**, 202 (2018)
208. H.An, H.W.Lee, B.K.Kim, J.W.Son, K.J.Yoon, H.Kim, J.H.Lee. *Nat. Energy*, **3**, 870 (2018)